Ocean Modelling 191 (2024) 102429

Contents lists available at ScienceDirect

Ocean Modelling

journal homepage: www.elsevier.com/locate/ocemod

Dependence of dense filament frontogenesis in a hydrostatic model

Yalin Fan [a,*], Zhitao Yu [a,b], Peter Sullivan [c], Adam Rydbeck [d]

[a] US Naval Research Laboratory, Stennis Space Center, MS 39529, United States
[b] Currently at National Marine Fisheries Service, Northeast Fisheries Science Center, Ecosystems and Aquaculture Division, Narragansett, RI 02882, United States
[c] National Center for Atmospheric Research, Boulder, CO 80307, United States
[d] Formerly at US Naval Research Laboratory, United States

ARTICLE INFO

Keywords:
Hydrostatic model
Frontogenesis
Langmuir turbulence parameterization
Horizontal mixing parameterization
Horizontal resolution

ABSTRACT

In this study, a hydrostatic model - the Navy Coastal Ocean Model (NCOM) is used to analyze the temporal evolution of a cold filament under moderate wind (along / cross filament) and surface cooling forcing conditions. The experimental framework adhered to the setup used in large eddy simulations by Sulllivan and McWilliams (2018). For each forcing scenario, the impact of horizontal resolutions is systematically explored through varies model resolutions of 100 m, 50 m, and 20 m; and the influence of horizontal mixing is investigated by adjusting the Smagorinsky constant within the Smagorinsky horizontal mixing scheme. The role of surface gravity waves is also assessed by conducting experiments both with and without surface wave forcing.

The outcomes of our study revealed that while the hydrostatic model is able to predict the correct characteristics/physical appearance of filament frontogenesis, it fails to capture the precise dynamics of the phenomenon. Horizontal mixing parameterization in the model was found to have marginal effect on frontogenesis, and the frontal arrest is controlled by the model's subgrid-scale artificial regularization procedure instead of horizontal shear instability. Consequently, higher resolution is corresponding to stronger frontogenesis in the model. Thus, whether the hydrostatic model can produce realistic magnitude of frontogenesis is purely dependent on the characteristic of the front/filament simulated and model resolution. Moreover, examination of the parameterized effect of surface gravity wave forcing through vertical mixing unveiled a limited impact on frontogenesis, suggesting that the parameterization falls short in representing the real physics of wave-front interaction.

1. Introduction

Oceanic submesoscale structures usually have a horizontal scale of 1 to 10 km. They are inevitably crucial to bridging the *meso* and smaller scales (Thomas et al., 2008). At the submesoscale, the nonhydrostatic process start to kick in, but may or may not be significant depending on what phenomenon we are looking at Internal tides are examples where nonhydrostatic processes have significant influence, while the oceanic fronts may still be considered hydrostatic given their horizontal and vertical scales (Mahadevan 2006).

Fronts and filaments are very common to the ocean (Ullman and Cornillon 1999; Gula et al. 2014), and associated with narrow geostrophic jets and strong shear (Ferrari and Rudnick, 2000). Sub-mesoscale structures such as fronts and filaments are thought to be instrumental in transferring energy and properties from the largely adiabatic mesoscale flow field to a scale where mixing occurs (McWilliams 2003, Molemaker et al., 2005, Thomas et. al. 2008). While Fronts have been studied intensively both dynamically (Hoskins, 1982) and observationally (e.g., Rudnick and Luyten 1996; Rudnick 1996), research on filaments that have analogous dynamical processes (Hakim et al. 2002; Lapeyre and Klein 2006; McWilliams et al. 2009) are relatively limited (McWilliams et al. 2015, referred to M15 from here after).

Filaments play an important role in oceanic biogeochemistry, affecting both lateral and vertical transport of tracers like nutrients, phytoplankton, and zooplankton larvae (Lehahn et al. 2007). An isolated filament, once formed, can be in a hydrostatic, geostrophic, and stationary state when in the absence of nonconservative mixing or straining deformation (M15). Thus, theoretically, hydrostatic models should be sufficient in simulating the evolution of such filament.

Utilizing a 2D version of the Regional Oceanic Modeling System (ROMS) with parameterized boundary-layer mixing through the K-profile parameterization (KPP) developed by Large et al. (1994), M15 has illustrated that an initial dense filament in turbulent thermal wind (TTW) balance undergoes rapid frontogenesis. This process is

* Corresponding author.
E-mail address: yalin.fan.civ@us.navy.mil (Y. Fan).

https://doi.org/10.1016/j.ocemod.2024.102429
Received 29 February 2024; Received in revised form 5 August 2024; Accepted 27 August 2024
Available online 28 August 2024

characterized by a shrinking width and increasing cross-filament velocity and buoyancy gradients until the width approaches the model grid resolution scale, at which point the model's subgrid-scale regularization procedure artificially arrests further frontogenesis. While the authors identified vertical mixing as a crucial factor in inducing horizontal frontogenesis through secondary circulation, they cautioned that " no particular physical credence is given to the horizontal eddy diffusivities that represent the small-scale turbulence that causes the arrest until a more fully 3D simulation can discover what their proper cause might be." This caveat arises because the strong lateral gradients associated with the filaments violate the assumptions of KPP, which considers the turbulence field to be horizontally homogeneous, temporally stationary, or self-similarly developing. Consequently, this raises questions about the realism of the frontogenesis simulated in their model. As M15 highlighted, their 2D solutions exclude 3D instability processes that could potentially interrupt or even arrest the frontogenetic progression, or at the very least, transform it into more fragmented surface vorticity lines. Therefore, this study aims to delve into the life cycle of a dense filament to explore the capabilities of a full 3D hydrostatic model in simulating frontogenesis.

The best way to judge how well a model can accurately represent the realistic ocean dynamics and upper ocean structures is to compare the results with observations. However, the awkward size of dense filaments has presented an observational barrier: they are large for shipboard instrument detection, small and rapidly evolving for typical ship surveys, small for many satellite remote sensing footprints, and often difficult to distinguish from intertia-gravity waves in single-point time series or individual vertical profiles (McWilliams 2016).

With the continuous increase of computational power, researchers were able to use large eddy simulation (LES) models to simulate the evolution of density fronts and filaments and their interaction with boundary layer turbulence using large horizontal domains of ~10 km and with O(10^{10}) grid points. These LES models can resolve both the submesoscale currents and the dominant scales of the turbulence and fully encompasses their dynamical interaction. Typical studies of this type are Sullivan and McWilliams (2018, referred to SM18 here after) who examined the lifecycle of a cold (dense) filament undergoing frontogenesis in the presence of turbulence generated by surface stress and/or buoyancy loss using the NCAR LES, and Sullivan and McWilliams (2019, referred to SM19 here after) further investigated the impact of surface gravity waves on the strength of frontogenesis using the same model. The NCAR LES was demonstrated to be able to faithfully reproduce in situ observed transient evolution of physical/chemical states and dynamics of the upper ocean through several studies (e.g., Liang et al. 2020; Fan et al. 2018; Fan et al. 2020). Thus, in this study, we will use SM18 and SM19 as a baseline to evaluate a hydrostatic model's capability to realistically represent frontogenesis at a dense filament.

This study is presented in four sessions. The model details and design of numerical experiments conducted are given in Section 2; model results are analyzed in Section 3; and the conclusion is given in Section 4.

2. Method

2.1. Numerical model

The hydrostatic model used in this study is the Navy coastal ocean model (NCOM). This model integrates the primitive equations in time using an explicit leapfrog scheme with a split barotropic/baroclinic mode (Barron et al., 2006, Fan et al. 2021). It has a free surface and explicitly represents time-evolving temperature, salinity, velocity, and sea surface height. NCOM uses Smagorinsky horizontal mixing scheme (Smagorinsky 1963) and provides different options of second moment turbulent closure (SMTC) models for vertical mixing parameterization. In this study, we use the Mellor-Yamada level 2.5 model (Mellor and Yamada 1982) for simulations without surface wave forcing, and the Harcourt (2015) and Kantha & Clayson (2004) models that include the impact of Langmuir turbulence for simulations with surface wave forcing. The Mellor–Yamada level 2.5 model has been used in many ocean and atmosphere models during the past several decades. Although there are some major shortcomings of the method that lead to smaller critical Richardson number and shallower boundary layer depth (Canuto et al., 2001; Cheng et al., 2002), it is still popularly used because the scheme considers the energetics of the mixing explicitly by solving diagnostic and prognostic equations, respectively, for the turbulent kinetic energy (TKE) and turbulent length scale. Since these equations carry information about the time history of the turbulence and thus can account for both advection and diffusion of the TKE. As people gradually recognized the importance of surface gravity waves in upper ocean mixing through Langmuir turbulence, modifications are made to the Mellor–Yamada SMTC models to represent the effect of surface waves. Kantha and Clayson (2004) is one of the first studies to add vortex forcing to the Mellor–Yamada type SMTC model to represent the effect of surface waves, and their scheme has been adapted into several ocean circulation models. Later on, Harcourt (2015, hereafter H15) further improved the SMTC model by incorporating the vortex forcing in the stability equations as well. These Langmuir enhanced mixing schemes produce stronger mixing in the water column. As a result, the mean currents become more uniformly distributed with depth, and this will consequently lead to changes in the horizontal variation of the currents. As demonstrated through model and observation comparisons at Ocean Stations Papa (Fan et al. 2021) and off North Carolina coast (Savelyev et al. 2022), the Harcourt (2015) parameterization provides the most significant impact from Langmuir turbulence and the closest representation of observed ocean dynamics among the SMTC models implemented in NCOM.

The choice of model domain size is guided by results in M15, SM18, and SM19, and is set to be 38 km in the cross-filament direction (slightly larger than M15) and 5 km in the along-filament direction (slightly larger than SM18 and SM19). This allows the model to capture large scales of motion so that the geostrophic currents generated by the density filament are realistic in scale and magnitude, and ensure flow homogeneity in the down-front direction. Different horizontal resolutions (100 m, 50 m, 20 m) are used to investigate dependence of model solutions on grid spacing. The vertical extent of the model is set to be 250 m (same as the previous studies) with 100 layers. The vertical grid is logarithmically-stretched with 0.5 m resolution at the surface, and each layer is thicker than the layer above by a fixed percentage.

2.2. Experiments set up

Surface forcing prescriptions in the model experiments (Table 1) are designed following SM18 with a choice of south-to-north along filament wind (denoted as N), west-to-east cross filament wind (denoted as E), or surface cooling (denoted as C). The water side friction velocity is set to be u_*=0.01 m s^{-1} for the wind forcing cases. This is corresponding to a surface winds of 8.5 ms^{-1}. The surface cooling is prescribed as a heat flux of 100 Wm^{-2} out of the ocean, which is equivalent to a kinematic surface flux $Q_* = 2.38 \times 10^{-5}$ Km^{-1}s^{-1}. In all experiments, the forcing (either wind or heat flux) remains uniform across the whole model domain and constant throughout the simulation period. The Coriolis parameter equals to $7.81 \times 10^{-5}\ s^{-1}$, equivalent to 32 N. In each forcing scenario, the effect of different horizontal resolutions is tested using 100, 50, and 20 m resolutions. We also investigated the effect of horizontal mixing by changing the Smagorinsky constant in the Smagorinsky horizontal mixing scheme, and the effect of surface gravity waves by running experiments with and without the surface wave forcing.

In simulations with surface wave effect, wave parameters are chosen to match those used by SM18, where the Stokes drift is given by a simple monochromatic profile $|u^s| = (ak)^2 c exp(2kz)$. In the equation, the wave slope ak = 0.1, wavelength λ = 60 m, wavenumber $k = \frac{2\pi}{\lambda} = 0.104\ \ m^{-1}$ and phase speed $c = 9.68$ ms^{-1} based on linear dispersion relationship.

Table 1
Simulation cases where C stands for surface cooling; N and E denote simulations driven by down-filament/across-filament winds; and lower-case e and n represent whether the surface waves direction is across-filament or down-filament. t_m is the time when $\langle\zeta\rangle_p$ reaches its maximum value, L_w is the average horizontal width of the front at t_m, and C_{smag} is the Smagorinsky constant for the Smagorinsky horizontal mixing scheme given in Eq. (3).

	Case	Resolution (m)	C_{smag}	Wave direction	t_m (hour)	L_w (m)
Surface	C100	100	0.1	–	5.9	170
Cooling	C50–0	50	0	–	5.9	110
	C50	50	0.1	–	5.7	110
	C50–0.2	50	0.2	–	5.7	110
	C50+*n*	50	0.1	North	5.5	120
	C50+*e*	50	0.1	East	5.5	120
	C20	20	0.1	–	4.5	80
Northward /	N100	100	0.1	–	5.8	270
Along	N50–0	50	0	–	5.5	190
Filament	N50	50	0.1	–	5.5	190
Wind	N50–0.2	50	0.2	–	5.5	190
	N50+wav	50	0.1	North	5.5	190
	N20	20	0.1	–	5.1	100
	E100	100	0.1	–	5.3	300
Eastward /	E50–0	50	0	–	5.1	250
Cross	E50	50	0.1	–	5.1	250
Filament	E50–0.2	50	0.2	–	5.1	240
Wind	E50+wav	50	0.1	East	5.0	250
	E20	20	0.1	–	4.8	180

The turbulent Langmuir number for this choice of parameters is then $La_t = \sqrt{u_*/|u^s|} \sim 0.32$, indicating a turbulent regime where wave effects are important in the absence of submesoscale influences (McWilliams et al. 1997).

The initial structure of the mean buoyancy field and the resulting geostrophic pressure gradients associated with the dense filament in NCOM is generated using turbulent thermal wind (TTW) balance following the design in M15 (Section 4b) and SM18 (Appendix A). Specifically, our prescription of the cross-front buoyancy variation $b_s(x)$ at the surface follows the smooth function in SM18, $b_s(x) = b_0 - \delta b_0 \exp\left[-(x/L)^2\right]$, where b_0 is a constant background value, δb_0 is the buoyancy jump set to be 0.785×10^{-3}ms^{-2}, and L is the front scale set to be 2 km. These values result a temperature jump of 0.48 K across a symmetric filament of 4 km wide (2 L). The structure and strength of this filament is constructed based on the intense submesoscale cold filaments formed on the subtropical gyre, interior wall of the Gulf Stream in the high-resolution Regional Oceanic Modelling System (ROMS) simulation conducted by Gula et al. (2014). The resulting field has similar deep stratification as in Gula et al. (2014), but the filament and boundary layer mixing strength are a bit weaker.

A two-step procedure is used to initialize the cold filament in the model as outlined in SM18. First, in step 1, simulations are started with a homogenous ocean at rest, i.e. the frontal parameters are set to zero. The mixed layer depth, defined as the depth at which the surface temperature cools by 0.2 °C, is $h_m = 66.5$ m, being consistent with SM18. The model is integrated for 48 h to establish the flow field and turbulence. A restart file is written at the end of the simulations. Vertical profiles of the average horizontal currents (u, v) for cases E50 and N50 after the 2-day simulations are shown in Fig. 1. The averaging is conducted over the entire horizontal domain within one inertial period (22.35 hour) at the end of the simulation. While the vertical distribution is consistent with M15 and SM18, the magnitude of the currents is relatively smaller than SM18 indicating weaker momentum transfer in NCOM compared to the LES. The horizontal currents for the cooling simulations are zero and thus not shown. Changing grid resolution does not change the current profiles.

Next, in step 2, the following modifications are made to the restart file in step 1: (1) a three-layer horizontal and mean vertical frontal structure b(x, z) is generated using TTW balance as designed in M15 (Section 4b); (2) a mean current field associated with the frontal structure, $\vec{u}(x, z)$, is calculated by the TTW relations following the procedure outlined in the appendix of M15; (3) the three-dimensional buoyancy and current fields in the restart file is reconstructed by adding the turbulent buoyancy and current fluctuations at the end of simulation in step

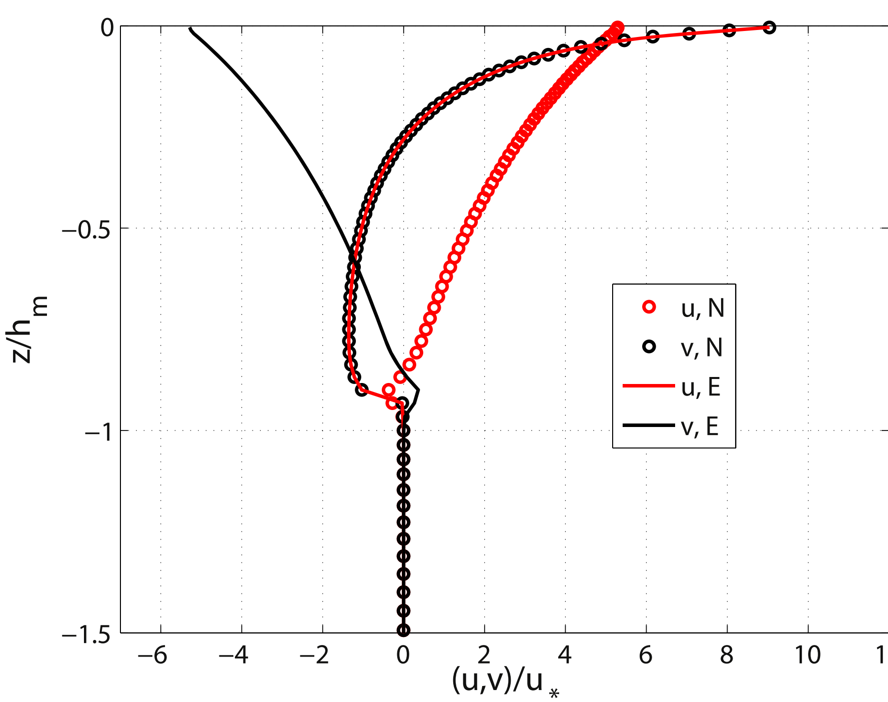

Fig. 1. Averaged currents normalized by friction velocity u_* from the pre-front runs (step 1) for experiments with northward (open circles) and eastward (solid lines) winds. The vertical coordinate is depth normalized by mixed layer depth, $h_m = 66.5$ m. The velocity profiles are calculated by averaging over the entire horizontal domain for one inertial period of 22.3 h. Because of the rotational symmetry of the horizontally homogeneous problem, (u, v) from eastward wind experiments equals (v, -u) from northward wind experiments.

1 to the mean frontal structure b(x, z) and $\vec{u}(x, z)$ (Note that b and $\vec{u}$ are uniform in the y direction). The new restart file contains realistic turbulent fields plus the desired mean buoyancy and current field. Then a 48-hour NCOM simulations are conducted starting from the modified restart file. Down front average or 'y' average, denoted by $\langle \cdot \rangle$, and their fluctuations from the mean, denoted as $(\cdot)'$, are used to diagnose the mean and turbulence fields of buoyancy and currents:

$$\vec{u}(x,y,z,t) = \langle\vec{u}\rangle(x,z,t) + \vec{u}'(x,y,z,t) \tag{1}$$

$$b(x,y,z,t) = \langle b\rangle(x,z,t) + b'(x,y,z,t) \tag{2}$$

3. Results

We will mainly focus on analyzing the results with 50 m resolution since the magnitude of $\langle\zeta\rangle_p$ in these simulations are most close to SM18.

3.1. Initial mean circulation

Secondary circulations (SC) are developed quickly at the beginning of the simulation. Snapshots of the averaged fields of temperature and velocity in an x–z plane are given in Figs. 2– 4 for cases E50, N50, and C50 at simulation hour 2. Besides the fronts are a bit wider than SM18, we see very similar frontal structures between the two studies: a cold dense filament with a width of ~4 km (2 L) and a boundary layer extended to ~66 m depth; down-front/up-front currents ⟨v⟩ on the left/right side of the front center line ($x = 0$); secondary currents ⟨u, w⟩ are developed in the boundary layer that feature a broad central down-welling jet at the middle and weaker upwelling in the far field on both sides; the temperature and vertical velocity fields are even-symmetric about the center line ($x = 0$) for all cases; while the horizontal velocity ⟨u, v⟩ fields are odd-symmetric in the surface cooling experiment (Fig. 4), there is significant asymmetry in these fields in the wind forcing cases (Figs. 2 and 3) due to the wind generated Ekman boundary layer currents. Changing of model resolution does not change the strength or structure of the filament at this stage for all forcing cases (Figs. A1-A6) except the presence of high frequency noise for higher resolution simulations.

3.2. Frontogenetic progression

The lifecycle of frontal onset, arrest and decay is analyzed in Fig. 5 through the time evolution of peak vertical vorticity $\langle\zeta\rangle_p = \partial_x\langle v\rangle$, its cross-front location χ_p, and the turbulent kinetic energy (TKE) at the time and location of $\langle\zeta\rangle_p$. Here, we follow M15 and SM18 to use vertical vorticity as an informative metric for frontal tendency. The results shown in Fig. 5 are for the 50 m resolution cases, without surface wave forcing, and using Csmag=0.1. Following SM18, these are surface layer statistics obtained by y-averaging along with vertical averaging over the top 5 m.

We can see $\langle\zeta\rangle_p$ starts at the same level as SM18 for all cases, stays flat during the onset phase ($t < 2$ h), undergoes a rapid intensification reaching its maximum values between hour 4 and 6 indicating the occurrence of frontogenesis in each simulation, and then followed by a much longer quasi-steady arrest and decay over the next ~10 hour. So, in general, in our simulations, we see the turbulent fluxes drive opposing secondary circulations, and these secondary circulations sharpen the across-filament current gradients which promotes further down-welling at the filament center. This positive feedback between turbulence, down-welling and SC leads to rapid frontogenesis, being consistent with M15 and SM18.

While the evolution of $\langle\zeta\rangle_p$ and the timing to reach its maximum value in our simulations are similar to SM18, the magnitude of $\langle\zeta\rangle_p$ is a bit different. Moreover, while a notable contrast is observed between the two different wind forcing scenarios in SM18, with $\langle\zeta\rangle_p$ displaying rapid growth and peaking nearly threefold in the northward wind case compared to the eastward wind case, the disparity between the two NCOM simulations utilizing distinct wind forcing is quite small.

According to SM18, a pair of closely matched SC of similar amplitude in a warm–cold–warm filament is more effective in creating a coherent downwelling jet thus leading to enhanced frontogenetic amplification such as in the surface cooling cases (C50m, Fig. 4). The authors further noted that strongly mismatched SC cells of different strength, as created by a cross-filament wind, leads to much lower values of $\langle\zeta\rangle_p$, and the moderate asymmetry of SC in the down-filament wind cases lead to a moderate amplification of frontogenesis. Notice that although the asymmetry of SC in E50 is a bit stronger than N50 in the NCOM simulations, the difference is smaller than that in SM18, and hence may be one of the reasons that lead to smaller contrast in the maximum $\langle\zeta\rangle_p$ values. As discussed in M15 and SM18, the asymmetry of SC in the wind forcing cases are due to the superposition of Ekman boundary-layer currents to the symmetric SC patterns as in the surface cooling cases. The weaker Ekman boundary-layer currents in the NCOM simulations (Fig. 1) has resulted in smaller difference in the SC asymmetry, and thus is one possible reason for the close values of $\langle\zeta\rangle_p$ for the two wind forcing cases.

Also notice that although NCOM predicted the highest peak vorticity in the surface cooling case being consistent with SM18, the decay in the cooling case is much faster than the wind forcing cases. To better understand this, we analyze the evolution of the kinetic energy conversion terms in the next section.

3.3. Filament instability

There are four energy conversion terms associated with the filament evolution as suggested by Gula et al. (2014) and SM18. The energy conversion from mean to perturbation kinetic energy (K_mK_e) is the sum of horizontal shear production HRS and vertical shear production VRS:

$$HRS = -\overline{u'^2}\frac{\partial\overline{u}}{\partial x} - \overline{u'v'}\frac{\partial\overline{u}}{\partial y} - \overline{v'^2}\frac{\partial\overline{v}}{\partial y} - \overline{u'v'}\frac{\partial\overline{v}}{\partial x} \tag{3}$$

$$\mathrm{VRS} = -\overline{u'w'}\frac{\partial\overline{u}}{\partial z} - \overline{v'w'}\frac{\partial\overline{v}}{\partial z} \tag{4}$$

The third term is buoyancy production that represents eddy potential to eddy kinetic energy conversion,

$$P_eK_e = \overline{w'b'} \tag{5}$$

and the last term P_mK_m represents the mean potential to mean kinetic energy conversion:

$$P_mK_m = \overline{w}\overline{b} \tag{6}$$

Time evolution of these four terms is presented for the surface cooling case (C50), along filament wind case (N50), and cross filament wind case (E50) at t_m when the maximum peak vertical vorticity was achieved, shortly after frontal arrest at simulation hour 7 and in the middle of the frontal decay stage at simulation hour 10 in Fig. 6. These are averaged statistics obtained by averaging horizontally in the y-direction and averaged vertically over the top 40 m. We can see that the mean potential to mean kinetic energy conversion (P_mK_m) dominate the kinetic energy field in all cases and at all times. While the magnitude of P_mK_m in our study is comparable with the ROMS results in Gula et al. (2014), they were several times smaller than the LES results in SM18. Notice that the cross-filament structure of P_mK_m is similar among the three studies.

Significant differences are observed in the shear production terms between the NCOM results in Fig. 6 and the LES results in SM18 at t_m. In the LES simulations, HRS and VRS has similar magnitude as P_mK_m and are shown to be the major mechanism to convert mean kinetic energy to TKE for the along filament wind forcing/surface cooling cases and the cross-filament case respectively. However, in the NCOM simulations,

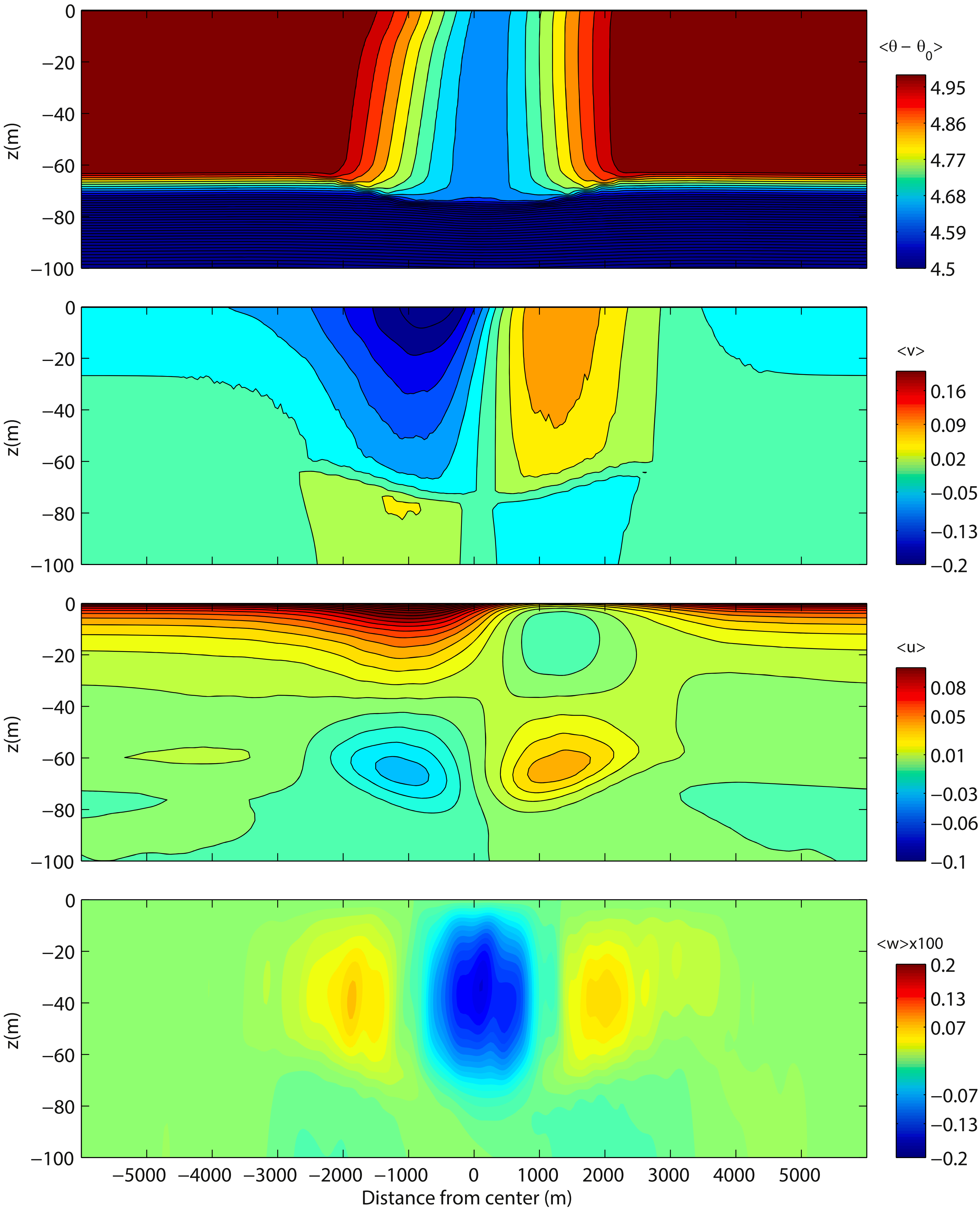

Fig. 2. Snapshots of averaged fields in an x–z plane for case E50 at simulation hour 2. The panels from top to bottom are: temperature anomaly ($\langle\theta - \theta_0\rangle$) in K, down-front velocity $\langle v\rangle$ in m s^{-1}, cross-front velocity $\langle u\rangle$ in m s^{-1} and vertical velocity $\langle w\rangle$ in m s^{-1}.

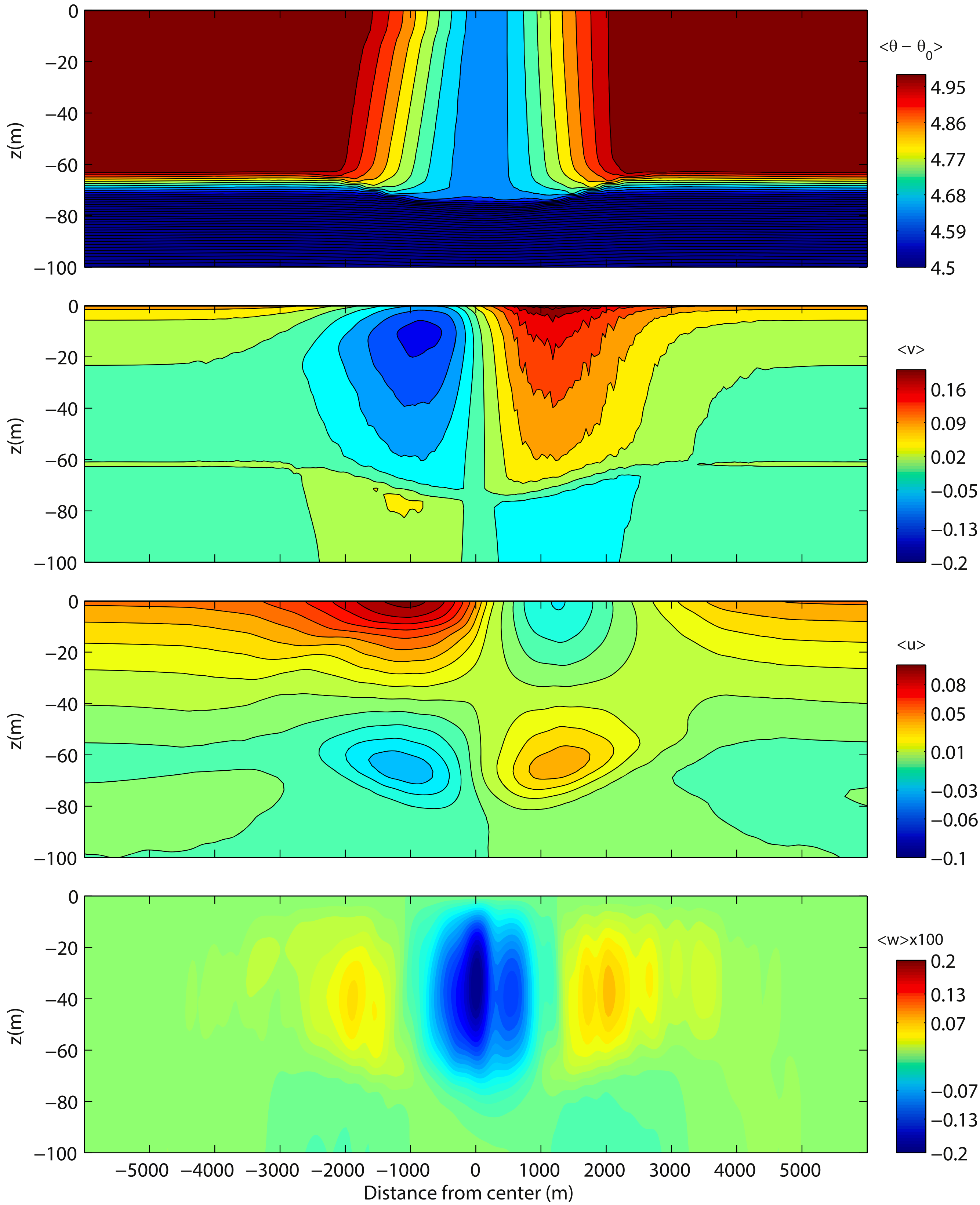

Fig. 3. Snapshots of averaged fields in an x–z plane for case N50 at simulation hour 2. The panels from top to bottom are: temperature anomaly ($\langle\theta - \theta_0\rangle$) in K, down-front velocity $\langle v\rangle$ in m s^{-1}, cross-front velocity $\langle u\rangle$ in m s^{-1} and vertical velocity $\langle w\rangle$ in m s^{-1}.

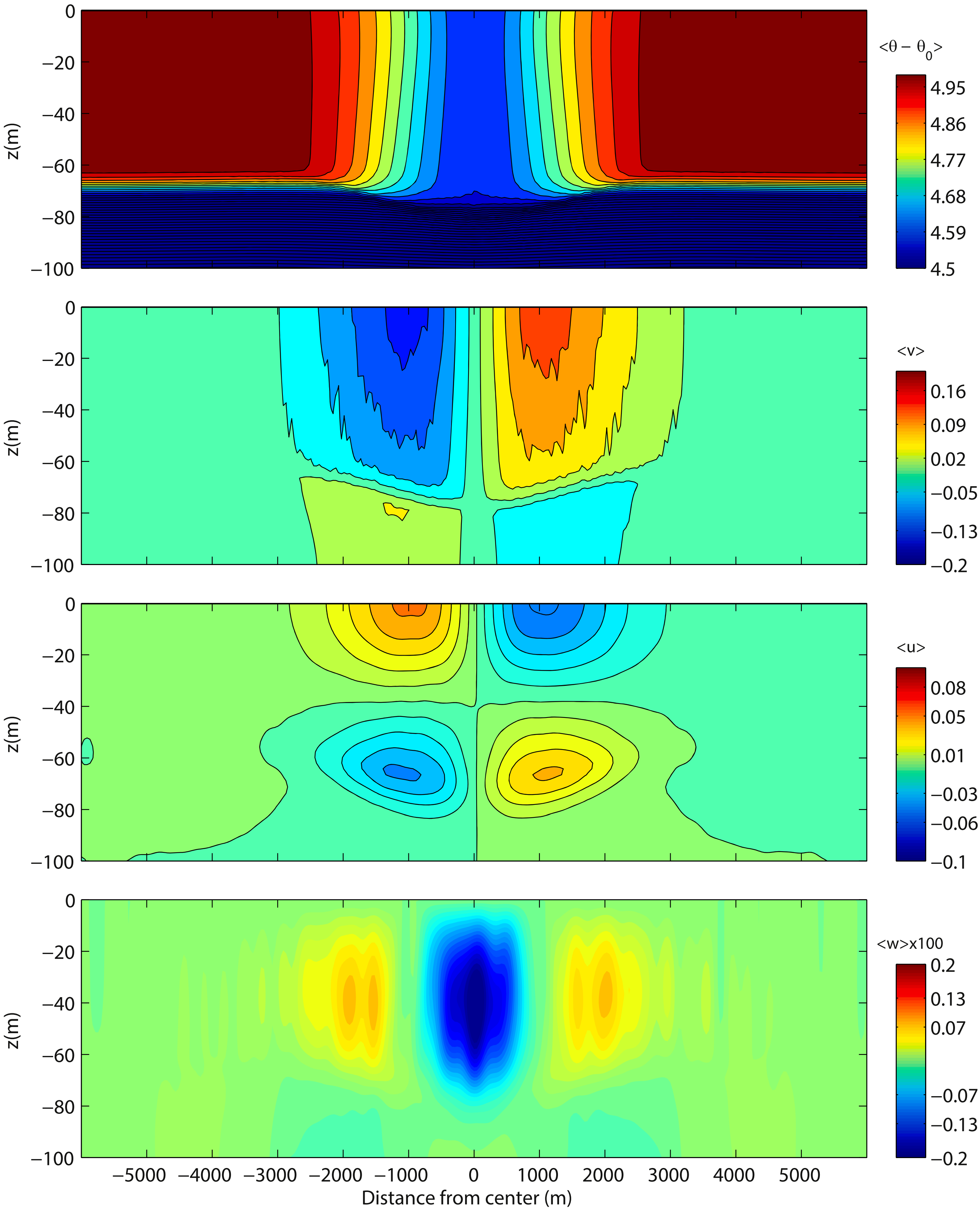

Fig. 4. Snapshots of averaged fields in an x–z plane for case C50 at simulation hour 2. The panels from top to bottom are: temperature anomaly ($\langle\theta - \theta_0\rangle$) in K, down-front velocity $\langle v\rangle$ in m s^{-1}, cross-front velocity $\langle u\rangle$ in m s^{-1} and vertical velocity $\langle w\rangle$ in m s^{-1}.

VRS in near zero in all cases. HRS is only observed in the surface cooling case, where it emerges during frontogenesis and the portion of energy conversion through this term grows with time (Fig. 6a, b, and c). This has led to perturbation to the filament and accelerated its decay compared with the wind forcing cases, being consistent with findings in Gula et al. (2014) who found that the barotropic instability is dominant over the baroclinic instability because of the strong horizontal gradients induced by a filament. However, not only the turbulent energy generated by HRS is much weaker in our surface cooling experiment, the barotropic instability is not observed in the wind forcing only cases in our study. A possible reason could be that the Gula et al. (2014) analysis is conducted at filaments that are already distorted and forced by the combination of time varying wind shear and buoyancy flux, while the filaments in our study are initially two dimensional with minimum distortion over time and forced by either constant wind shear or buoyancy flux. It is also worth noticing that while HRS dominate over VRS in both the along filament wind forcing and surface cooling cases in SM18, VRS is much stronger than HRS in the SM18 study contradicting to the findings in Gula et al. (2014).

Although both Gula et al. (2014) and SM18 found the buoyancy production term to be small compared with other terms, this term in all of our simulations is near zero indicating no fluctuating potential energy is converted to TKE in our simulations.

3.4. Energetics of the filament

The second thing we want to point out is the significant differences in the TKE magnitude between the NCOM results and SM18. In SM18, the TKE evolution follows the peak vorticity closely with strong intensification at the same time as the peak vorticity intensification. The authors noted that the main source of the TKE is horizontal shear production in the LES simulation with the arresting turbulence originate from the

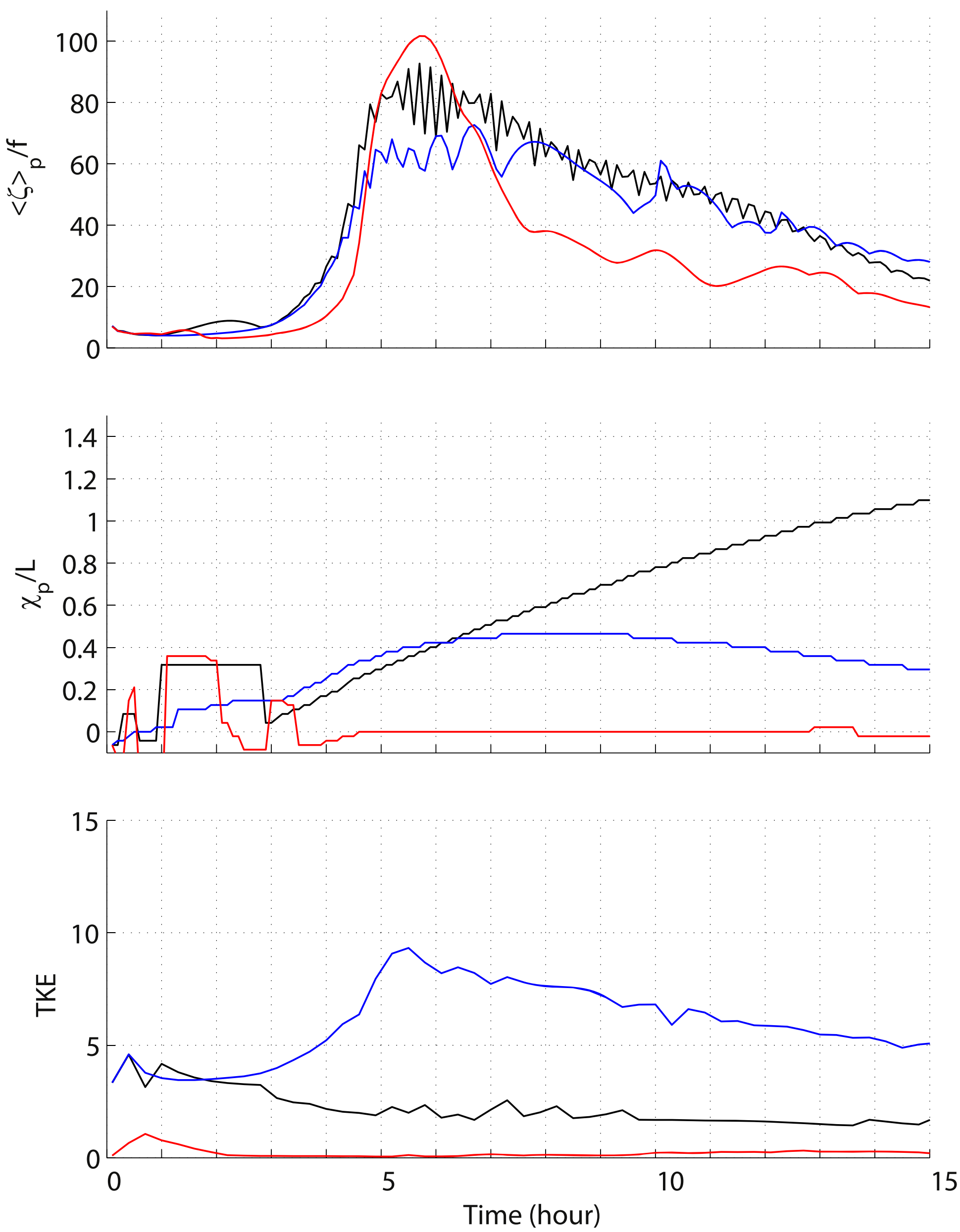

Fig. 5. Normalized peak average vertical vorticity $\langle\zeta\rangle_p/f$ (top panel), its cross-front location χ_p/L (middle panel), and turbulent kinetic energy TKE (bottom panel) as a function of time for the 50 m resolution cases listed in table 1. In the figure, black, blue, and red are corresponding to the northward wind, eastward wind, and surface cooling cases without wave forcing respectively. TKE is normalized by u_*^2 and w_*^2 for the wind forcing and surface cooling cases respectively.

fluctuating down-filament current, v'. It makes sense that TKE intensifies when the shear becomes stronger during frontogenesis. However, since NCOM cannot solve for turbulence in the model, the horizontal mixing is parameterized using the Smagorinsky scheme, in which the horizontal eddy viscosity is calculated as a function of the horizontal grid resolution and velocity shear:

$$\nu_\perp = C_{smag}\Delta x\Delta y\left(\left(\frac{\partial u}{\partial x}\right)^2 + \frac{1}{2}\left(\frac{\partial v}{\partial x}+\frac{\partial u}{\partial y}\right)^2 + \left(\frac{\partial v}{\partial y}\right)^2\right)^{1/2} \tag{7}$$

Where the Smagorinsky constant, C_{smag}, is ranging from 0.02 to 0.5. Large values of C_{smag} tend to over dissipate smaller features, where values that are too small can lead to excessive numerical noise and/or instability (Martin 2000). C_{smag} is set to be 0.1 in typical NCOM simulations according to Martin (2000) and the horizontal eddy diffusivity $\kappa_\perp$ is set to be equal to $\nu_\perp$. The same specifications are used for cases presented in Fig. 5.

The $\nu_\perp$ values after 2 h of model simulation and at t_m are plotted in Fig. 7 for the 50 m resolution cases without surface wave forcing. The horizontal mixing is relatively weak at the early state. As the cold filament undergoes rapid frontogenesis with shrinking width and increasing current shear, horizontal mixing is significantly enhanced near the center of the filament. The $\nu_\perp$ pattern and magnitude are very similar among the three forcing cases at the frontal arrest state with the maximum values concentrated within a few grid points at the center of the filament where the horizontal velocity shear is the largest.

In the early state (hour 2), stronger horizontal mixing is observed in the surface cooling case that occupies through the entire boundary layer and extends beyond the width of the cold filament. The magnitude and pattern of $\nu_\perp$ are comparable for all three cases near the filament center

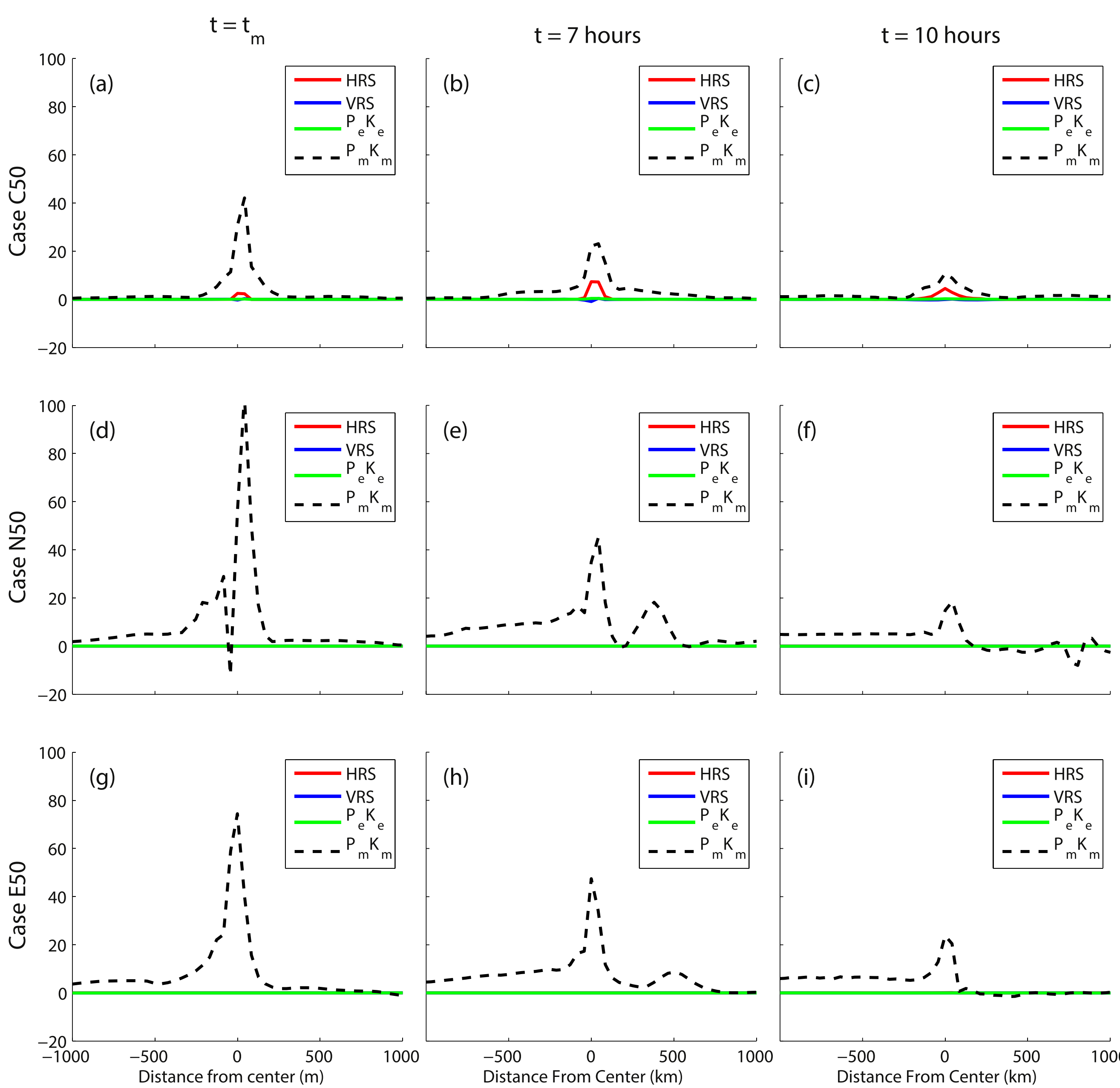

Fig. 6. Instantaneous local energy conversion profiles HRS (red), VRS (blue), P_eK_e (green), and P_mK_m (black dashed) computed for cases C50 (top panels), N50 (middle panels) and E50 (bottom panels) at t_m (left panels), simulation hour 7 (middle panels) and hour 10 (right panels). The Terms are normalized by $u_*^3/|h_i|$ in the wind forcing cases and by $w_*^3/|h_i|$ in the surface cooling case.

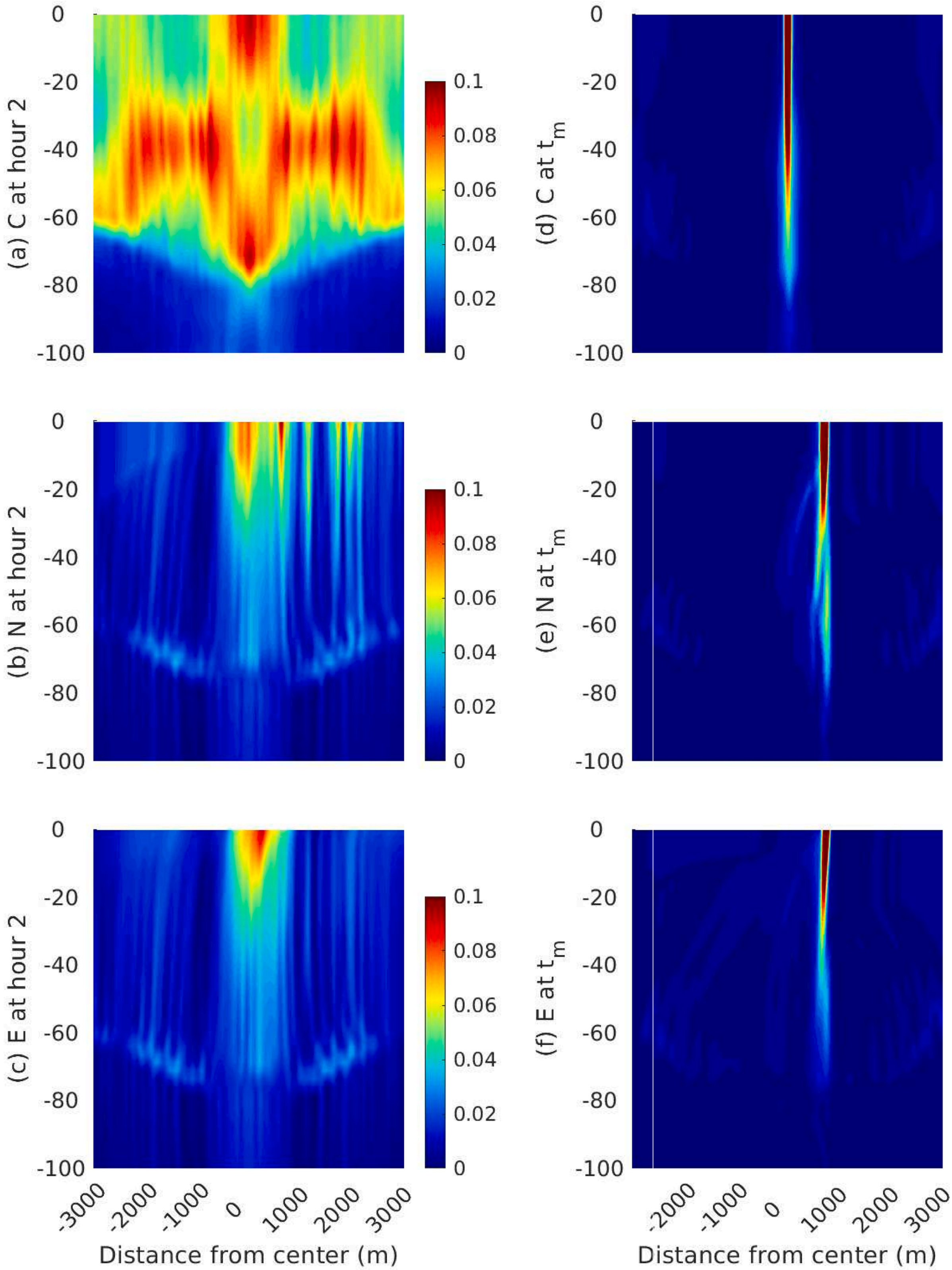

Fig. 7. Snapshots of averaged horizontal eddy viscosity ($\nu_{\perp}$) fields in an x–z plane for cases C50, N50, and E50 at simulation hour 2 (panels a, b, and c respectively), and at the time of maximum $\langle\zeta\rangle_p$ (panels d, e, f respectively). The variables plotted are normalized by w_*h_m for C50 and by u_*h_m for the wind forcing cases respectively.

and within the upper part of the boundary layer. The major difference between the surface cooling and wind forcing cases occur beneath 20 m indicating more active velocity fluctuations in depth through overturning induced by convection. Despite the differences among the three cases, horizontal mixing is very weak in all NCOM simulations compared with the LES results by Sullivan and McWilliams (2024) that shows significantly enhanced horizontal mixing during frontogenesis with large $\nu_{\perp}$ values two orders of magnitude higher than the values shown in Fig. 7.

To better understand the effect horizontal mixing in the frontal arrest, C_{smag} is set to be 0 and 0.2 in the 50 m resolution simulations without surface wave forcing (Experiments C50–0, C50–0.2, N50–0, N50–0.2, E50–0 and E50–0.2). The time evolution of peak vertical vorticity $\langle\zeta\rangle_p = \partial_x\langle v\rangle$, its cross-front location χ_p, and the turbulent kinetic energy (TKE) at the time and location of $\langle\zeta\rangle_p$ show very small dependence on the values of C_{smag} used in the simulation (Not shown). Note that larger values of C_{smag} are not tested in this study because they may lead to over dissipations and thus not practical for real ocean simulations (Mellor 1998, Soares et al. 2007).

The statistics of the runs are recorded in table 1, where the width of filament, L_w, is defined as the distance from the centerline where the flux divergence $\partial_x\langle u'v'\rangle$ first falls to zero outside of the filament zone. As shown by Sullivan & McWilliams (2024), $\langle u\rangle\partial_x\langle v\rangle \approx \partial_x\langle u'v'\rangle$. Since NCOM is a Hydrostatic model, it can better resolve the mean current value than the turbulent fluctuations. Thus, we choose to use the SC advection, $\langle u\rangle\partial_x\langle v\rangle$ as a proxi for $\partial_x\langle u'v'\rangle$, and define L_w as the distance from the centerline where $\langle u\rangle\partial_x\langle v\rangle$ first falls to zero outside of the filament zone.

From the statistical recorded in Table 1, minimum changes are observed with the changing C_{smag} values: there is no difference in the statistics for the along filament wind forcing cases; the filament width is a bit smaller with stronger horizontal mixing for the cross filament wind case; and the maximum vorticity is achieved at a slightly later time with no horizontal mixing in the surface cooling case with the filament width remained the same for different C_{smag} values. Overall, the differences due to C_{smag} value changes are too small to be considered important. Further increase Csmag may show larger differences, but it may lead to over dissipations at lower resolution simulations as suggested by previous studies. It is important to note that the experiments conducted in this study can only represent the evolution of an initially two-dimensional, dense, surface-layer filament with certain strength under a constant moderate wind or buoyancy forcing. While it is possible to adjust the C_{smag} values to achieve results that closely resemble those obtained from Large Eddy Simulations (LES), such an approach becomes impractical for real ocean simulations conducted at varying horizontal resolutions—often coarser than the resolution used in this study. Realistic scenarios involve the interaction with fronts and filaments exhibiting a wide range of strengths, as well as exposure to diverse meteorological forcings. The key takeaway here is the necessity to develop a more comprehensive horizontal mixing parameterization.

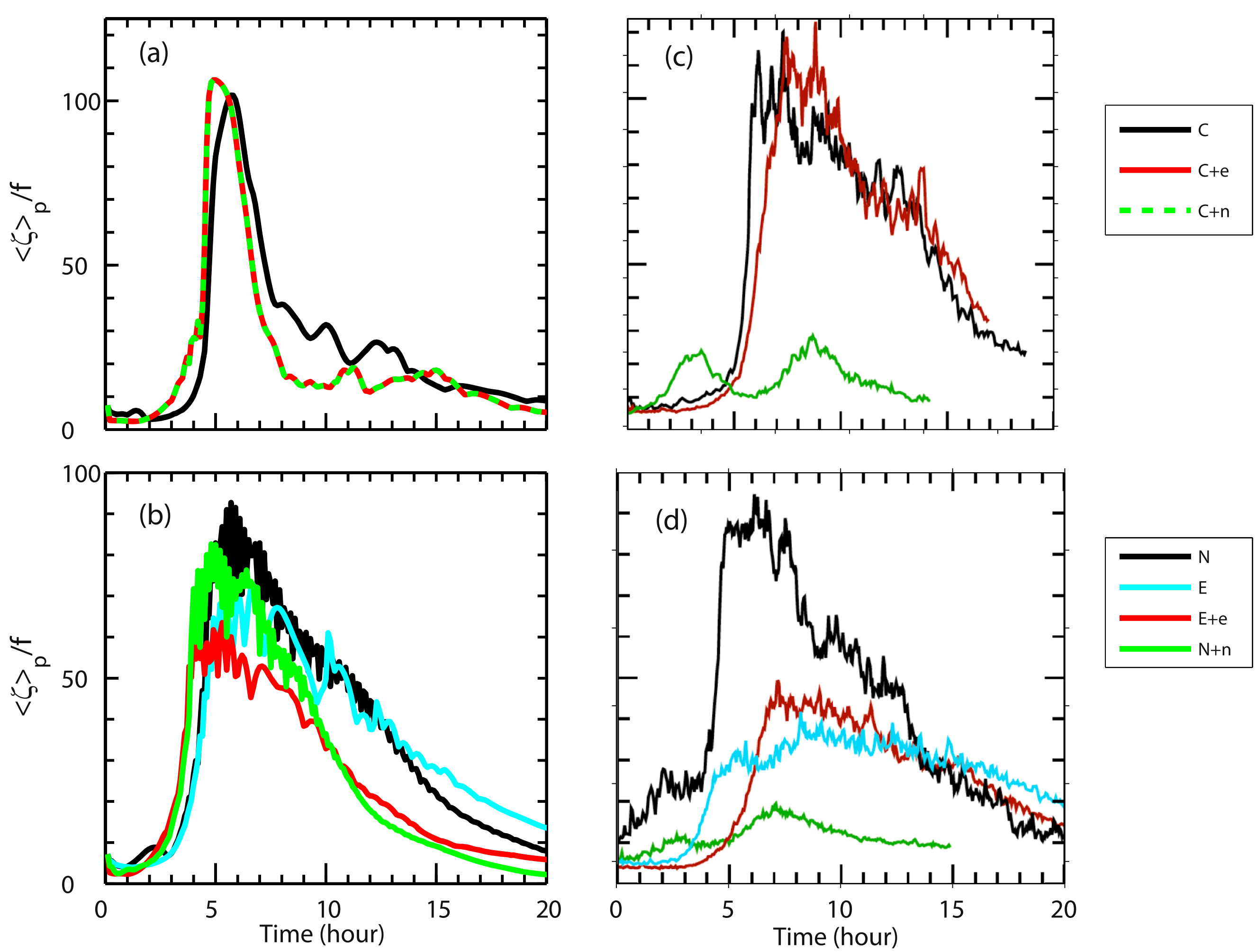

Fig. 8. Time variation of averaged normalized peak vertical vorticity $\langle\zeta\rangle_p/f$ near the water surface for simulations driven by surface cooling and waves (C; C + e; C + n) from (a) NCOM and (c) LES in model, and simulations driven by winds and waves (N; $N + n$; E; $E + e$) from (b) NCOM and (d) LES model. LES model Results in panel (c) and (d) are obtained from Fig. 3 of Sullivan and McWilliams (2019).

This parameterization should accurately capture the enhanced mixing resulting from lateral shear instability during frontogenesis, rather than relying on the tuning of C_{smag} for specific case studies.

3.5. Effect of surface gravity waves

While impact of fronts and filaments on surface gravity wave characteristics are studies intensively (i.e. Holthuijsen and Tolman 1991, Fan et al. 2009, Abolfazli et al. 2020), research carried out on the impact of surface gravity waves on fronts and filaments is sparse. In the study of SM19, the authors found that surface gravity waves can have important impact on frontogenesis, and the strength of the effect is dependent on wave propagation direction relative to the filament axis (Fig. 8c, 8d). Down-filament winds and waves are found to be especially impactful. It was shown that the Langmuir circulation generated by the down-filament waves can dramatically altered the current structure across the filament and thus reduced the horizontal current shear. As a result, they can significantly reduce the peak level of the frontogenesis by fragmenting the filament into primary and secondary down-welling sites in a broad frontal zone. The horizontal composite vortex force is believed to be the main causes for these changes with the up-wave current generated by the Stokes–Coriolis effect as the secondary contributor.

As a general circulation model, vertical mixing is parameterized in NCOM to provide an idealized description of turbulence with a reasonable compromise between cost and accuracy. In this section, the Harcourt (2015) parameterization is used to evaluate the effect of parameterized Langmuir turbulence on frontogenesis by conducting NCOM experiments with and without Stokes drift forcing (Table 1).

From the comparisons in Fig. 8, we can see some noticeable differences in the time evolution of peak vertical vorticity $\langle\zeta\rangle_p$ with and without wave forcing in the NCOM simulations. While the changes in $\langle\zeta\rangle_p$ brought by the cross-filament wave is similar between NCOM and LES results, the reduction in $\langle\zeta\rangle_p$ due to down-filament wave forcing is significantly smaller in the NCOM results than what is observed in the LES results. Furthermore, the effect of cross- and down-filament wave forcing are exactly the same for the surface cooling case.

Although the Harcourt (2015) parameterization added vortex forcing to the Mellor–Yamada type of SMTC model to represent the effect of Langmuir turbulence induced by nonlinear interaction between surface

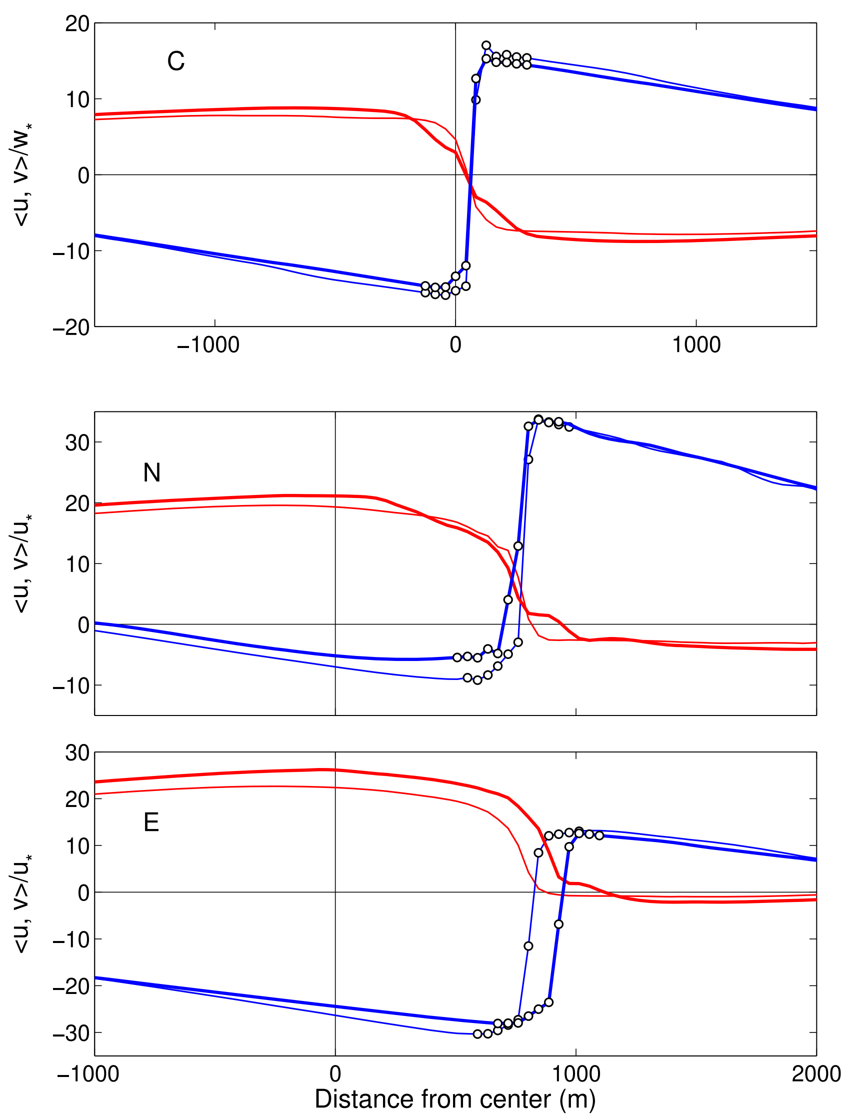

Fig. 9. Across-filament variation of currents $\langle u\rangle/u_*$ (red lines) and $\langle v\rangle/u_*$ (blue lines) for simulations driven by surface cooling (C, upper panel), down-filament wind (N, middle panel), and cross-filament wind (E, bottom panel). The currents in simulations E, N, C are normalized by u_*, u_*, and w_* respectively. In each panel, thin / thick lines are results from simulations without / with surface wave forcing. The black circles with white face on the blue lines represent location of grid point along the cross section of the filament on the two sides of the filament center.

gravity waves and wind driven currents, turbulent mixing is enhanced in the model in the form of increased vertical eddy viscosity/diffusivity in the water column. The parameterization can help to obtain a more well-mixed surface layer, and hence more uniformly distributed mean currents with depth and reduced vertical shear. In another words, this parameterized effect of Langmuir turbulence is only limited in the vertical direction, and thus the NCOM model results are more aligned with SM18 rather than SM19. While the horizonal currents may be affected indirectly through advection, the impact is quite small. This is generally the case for other SMTC models (such as the Kantha and Clayson 2004 as demonstrated in Appendix B) and KPP schemes (such as Li and Fox-Kemper 2017, Large et al. 2019, Solano and Fan 2022, etc.) as well that parameterize Langmuir turbulence through enhanced vertical mixing. Thus, although the interaction between Langmuir circulation and current shear can significantly altered the current structure across the filament and reduced the horizontal current shear in the LES simulations, changes in the horizontal current structure in the NCOM simulations are only generated due to the vertical redistribution of horizontal currents by the enhanced vertical mixing, and are much smaller in magnitude (Fig. 9) compared with SM19. Apparently, the parameterized Langmuir turbulence through vertical mixing cannot produce the same effect of the wave-current interaction as demonstrated in the LES model.

3.6. Effect of horizontal resolution

The effect of horizontal resolution on frontogenesis is investigated in this section. Notice the magnitude of $\langle\zeta\rangle_p$ is significantly lower/higher in the 100 m/20 m resolution cases compared to the 50 m cases (Fig. 10), the time it takes to reach its maximum value, t_m is longer/shorter (Table 1), and the width of the filament at arrest decreases with the increase of resolution. Unlike the LES model that resolves the turbulence down to meter scale, NCOM uses parameterized boundary-layer mixing. While the SMTC model seems to produce comparable vertical mixing to generate similar secondary circulations as in SM18, the horizontal diffusion is too weak to have any effect on frontal arrest as discussed in Section 3.4. Thus, the cold filament continues to undergo rapid frontogenesis with shrinking width and increasing cross-filament velocity and buoyancy gradients until the grid resolution is approached, i.e. the horizontal scale over which $<u, v>$ reverses sign (Fig. 9). Then the filament is damped by the horizontal diffusion when the filament scale

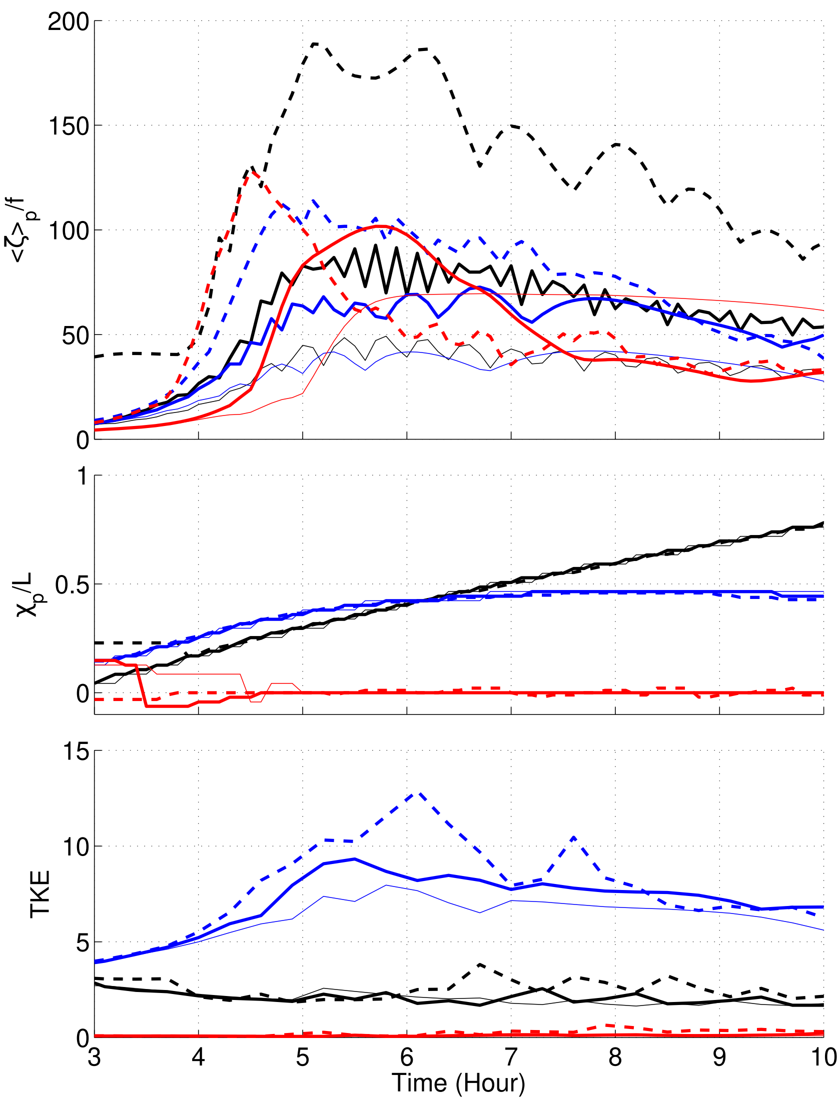

Fig. 10. Averaged normalized peak vertical vorticity $\langle\zeta\rangle_p/f$ (top panel), its cross-front location χ_p/L (middle panel), and turbulent kinetic energy TKE (bottom panel) as a function of time for all cases without surface wave forcings in table 1. In the figure, black, blue, and red are corresponding to the northward wind, eastward wind, and surface cooling cases respectively. Solid thin lines, solid thick lines, and dashed thick lines represent cases with 100 m, 50 m, and 20 m resolution respectively. TKE is normalized by u_*^2 and w_*^2 for the wind forcing and surface cooling cases respectively.

comes close to the grid scale, and the model's subgrid-scale regularization procedure artificially arrests further frontogenesis, being consistent with the findings in M15.

Note that while the 50 m and 100 m resolution experiments show the same behavior, the 20 m resolution experiments demonstrated a surprisingly different pattern with the down-filament wind case produces the highest $\langle\zeta\rangle_p$ that is almost twice as large as the other two cases (Fig. 10). Further investigation shows this phenomenon is simply due to the strong sharpening of horizontal momentum gradient at high resolution. While we can clearly see enhanced frontogenesis with higher resolution through the time evolution of $\langle\zeta\rangle_p$, the location of maximum vorticity and TKE barely changed with resolution. The dynamical and energetic evolution of the filament is consistent at all three resolutions.

4. Summary and discussion

Fronts and filaments are very common to the world ocean, especially in the coastal regions where various water masses, currents, and physical processes interact. They can have a significant impact on the dynamics and structure of the upper ocean. These fronts and filaments usually have a horizontal scale of O(1 km) or less, the nonhydrostatic process start to kick in as the resolved horizontal and vertical scale of the motion becomes comparable. However, due to computational limitations, hydrostatic models are usually used for coastal studies and predictions. Whether these models can correctly represent the frontogenesis is not well understood. In this study, a hydrostatic model - the Navy Coastal Ocean Model (NCOM) is used to analyze the time evolution of a cold filament under moderate wind (along / cross filament) and surface cooling forcing scenarios following the experimental set up in Sulllivan and McWilliams (2018). In each forcing scenario, the effect of different horizontal resolutions is tested using 100, 50, and 20 m resolutions. We also investigated the effect of horizontal mixing by changing the Smagorinsky constant in the Smagorinsky horizontal mixing scheme, and the effect of surface gravity waves by running experiments with and without the Stokes drift forcing.

The results indicate that the hydrostatic model can effectively predict the characteristics of filament frontogenesis but falls short in capturing the correct dynamics such as enhanced turbulence and energy dissipation as observed by D'Asaro et al. (2011) or intensified turbulent kinetic energy as demonstrated by Sullivan & McWilliams (2018) . The influence of horizontal mixing on frontogenesis in the model is minimal, with the front arrest being dictated by the model's subgrid-scale artificial regularization procedure rather than horizontal shear instability. Thus, higher resolution in the model corresponds to intensified frontogenesis.

The realism of frontogenesis in the hydrostatic model hinges on the simulated front/filament characteristics and the resolution of the model. It becomes evident that the hydrostatic model's ability to correctly capture the characteristics/physical appearance of frontogenesis is contingent on both these factors. However, as discussed earlier, hydrostatic models cannot correctly represent the dynamics behind frontogenesis, arrest and decay of the filament, and thus, in a sense, these models can never accurately fully reproduce frontogenesis.

A crucial insight arises from the fact that the prevalent horizontal and vertical mixing parameterizations in ocean general circulation models (OGCMs) were developed in an era when model resolutions were coarse (on the orders of 10 to 100 km). During this period, submesoscale currents were not resolved but rather represented by subgrid-scale processes. Furthermore, traditionally, most ocean boundary layer mixing models have been patterned after the atmospheric boundary layer models, including Smagorisk (1963) and Mellor and Yamada (1982), and have therefore ignored the fact that the air–sea interface is a nonrigid, mobile surface capable of sustaining gravity wave motions with all their attendant complex dynamics (Kantha and Clayson 2004).

People gradually recognized the importance of surface gravity waves in upper ocean mixing in the past few decades. Field observations in the mid-20th century revealed the significant impact of Langmuir circulations on vertical mixing, challenging existing models that underestimated this effect. The Craik-Leibovich (1976) theory provided a theoretical framework for understanding these interactions, while advancements in computational power and instrumentation enabled detailed simulations through LES models and high-resolution data collections. Various ocean surface boundary layer vertical mixing schemes with Langmuir turbulence enhancements have been proposed in the literature, including the Kantha & Clayson (2004) and Harcourt (2015) parameterization used in this study. However, we found that surface gravity wave forcing through vertical mixing, when parameterized, has a negligible impact on frontogenesis and fails to fully encapsulate the intricate physics of wave-front interaction. One limitation of these vertical mixing parameterizations is that they are all developed based on the assumption that the buoyancy field is horizontally uniform and thus cannot represent the interaction between boundary layer turbulence and submesoscale features, such as the wave-front interaction demonstrated in Sullivan and McWilliams (2019).

As our models increasingly achieve adequate resolution for submesoscale currents without relying on subgrid-scale representations, it unveiled limitations in the current mixing parameterizations, and there arises a pressing need for new mixing parameterizations. These should be designed to accurately capture the energy cascade resulting from interactions between submesoscale currents and small-scale turbulence (Fan et al. 2023).

While the development of these mixing parameterizations aimed to capture the effects of subgrid-scale processes, including submesoscale and small-scale turbulence interactions, our understanding of submesoscale and small-scale turbulence interactions remains incomplete, attributed to limitations in observational capabilities and computational resources. Although multiple studies have been conducted on the interaction between fronts/filaments and boundary layer turbulence using LES models (SM18, SM19, Hamlington et al. 2014; Yuan and Liang, 2021, etc.), the conditions in these studies are highly idealized. Idealizing and isolating individual processes makes it easier to study their effects, but can also unrealistically magnify or underestimate their impact, due to the lack of complex and nonlinear interactions of multiple dynamical processes taking place in the real ocean. However, fully resolving these processes in realistic ocean models that involve interactions among complex dynamical processes continues to pose a challenge.

It is important to note that both the experiments conducted in this study and the LES results presented in SM18 and SM19 can only represent the evolution of an initially two-dimensional, dense, surface-layer filament with certain strength and under a constant moderate wind or buoyancy forcing. While our findings provide valuable insights into the hydrostatic model's capability to simulate frontogenesis under controlled conditions, it is important to note that these conclusions are derived from idealized scenarios. Real ocean simulations, influenced by more complex and variable environmental factors, may yield different results. With the continuous increase of computational powers and advancement in observation techniques, validations with real-world data may become feasible in the near future.

CRediT authorship contribution statement

Yalin Fan: Writing – original draft, Visualization, Software, Resources, Methodology, Investigation, Funding acquisition, Formal analysis, Conceptualization. **Zhitao Yu:** Writing – review & editing, Visualization, Investigation. **Peter Sullivan:** Investigation, Investigation. **Adam Rydbeck:** Software.

Declaration of competing interest

The authors declare that they have no known competing financial interests or personal relationships that could have appeared to influence the work reported in this paper.

Data availability

Data will be made available on request.

Acknowledgments

We would like to express our appreciation to the anonymous reviewers for their constructive comments. Y. Fan and A. Rydbeck were funded by Office of Naval Research under program element 62435N work unit 6B63 and 62A1B6. Financial support for Z. Yu is provided by the "6.1 Dynamical controls of the East China Sea and Yellow Sea (ECSYS) upwelling and water masses'' project sponsored by the Office of Naval Research under program element 61153N. This paper is a contribution of NRL/JA/7320-24-6325, and has been approved for public release.

Appendix A. Averaged fields of temperature and currents

Snapshots of the averaged fields of temperature and velocity in an x–z plane for model experiments with horizontal resolutions set to be 100 m (A1 – 3) and 20 m (A 4 – 6). Surface gravity wave forcing is not applied in these experiments, and the Smagorinsky constant within the Smagorinsky horizontal mixing scheme is set to be 0.1. Comparing with the 50 m horizontal resolution experiments in Fig. 2– 4, we can see that changing of model resolution does not change the strength or structure of the filament at this stage for all forcing cases except the presence of high frequency noise for higher resolution simulations.

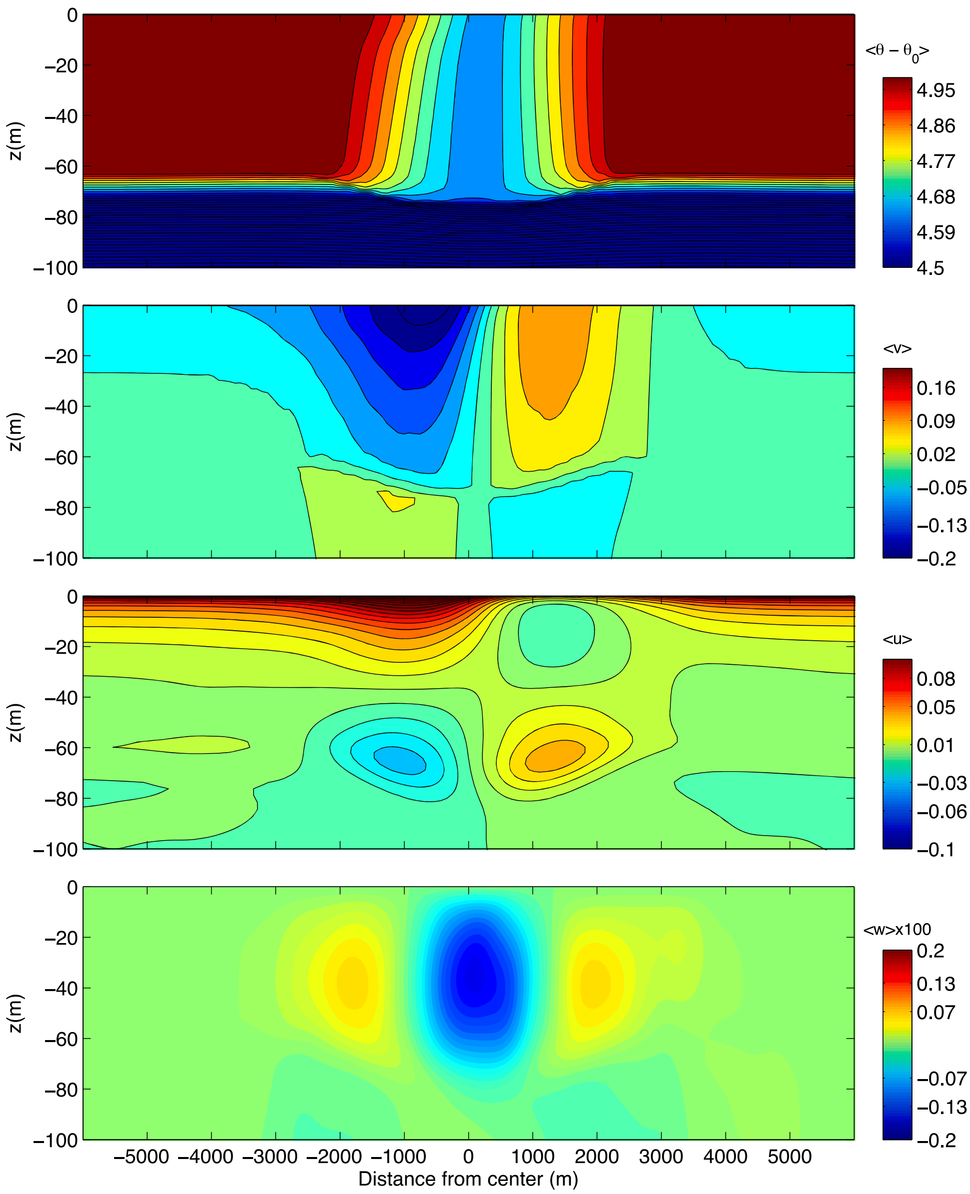

Fig. A1. Snapshots of averaged fields in an x–z plane for case E100 at simulation hour 2. The panels from top to bottom are: temperature anomaly ($\langle \theta - \theta_0 \rangle$) in K, down-front velocity $\langle v \rangle$ in m s^{-1}, cross-front velocity $\langle u \rangle$ in m s^{-1} and vertical velocity $\langle w \rangle$ in m s^{-1}.

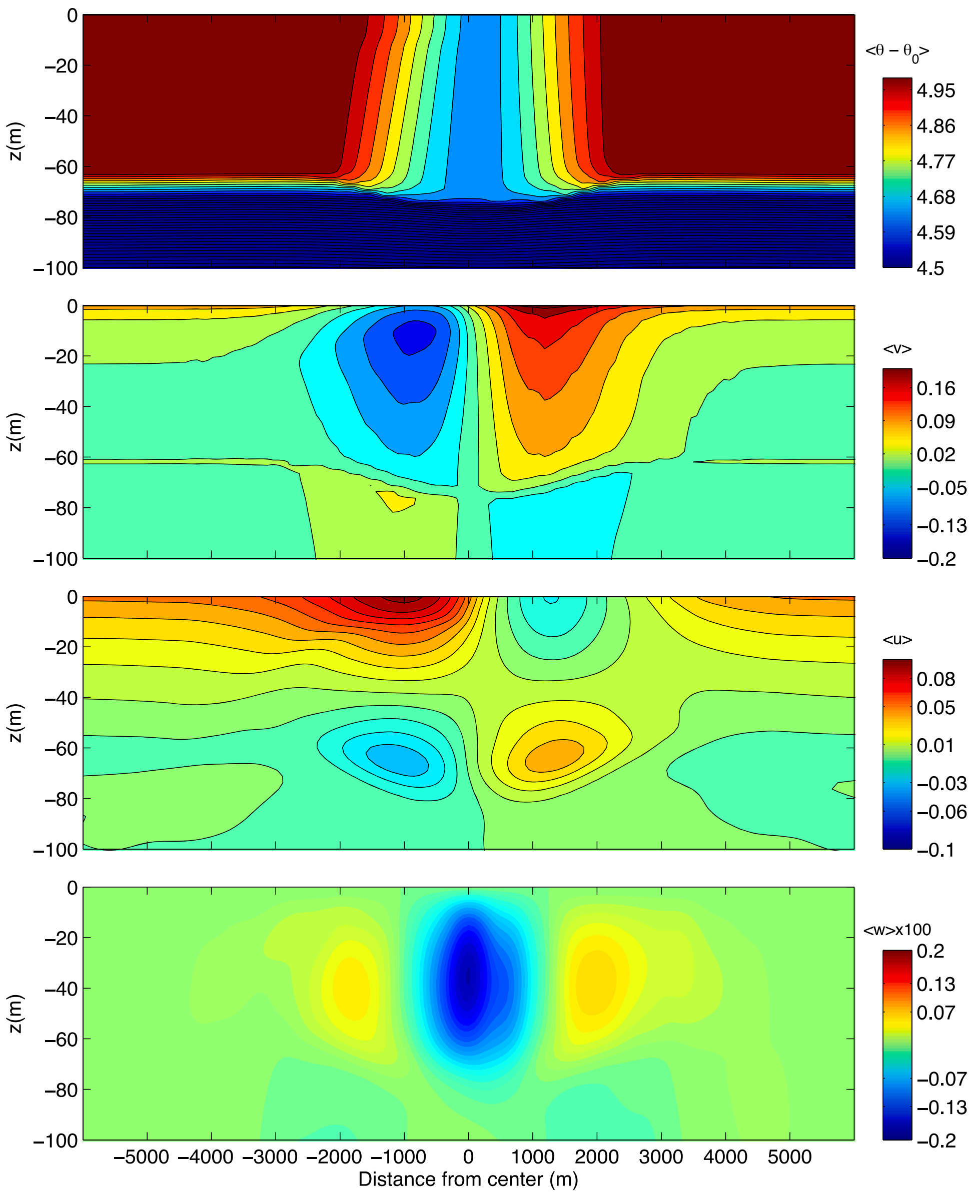

Fig. A2. Snapshots of averaged fields in an x–z plane for case N100 at simulation hour 2. The panels from top to bottom are: temperature anomaly ($\langle\theta - \theta_0\rangle$) in K, down-front velocity $\langle v\rangle$ in m s^{-1}, cross-front velocity $\langle u\rangle$ in m s^{-1} and vertical velocity $\langle w\rangle$ in m s^{-1}.

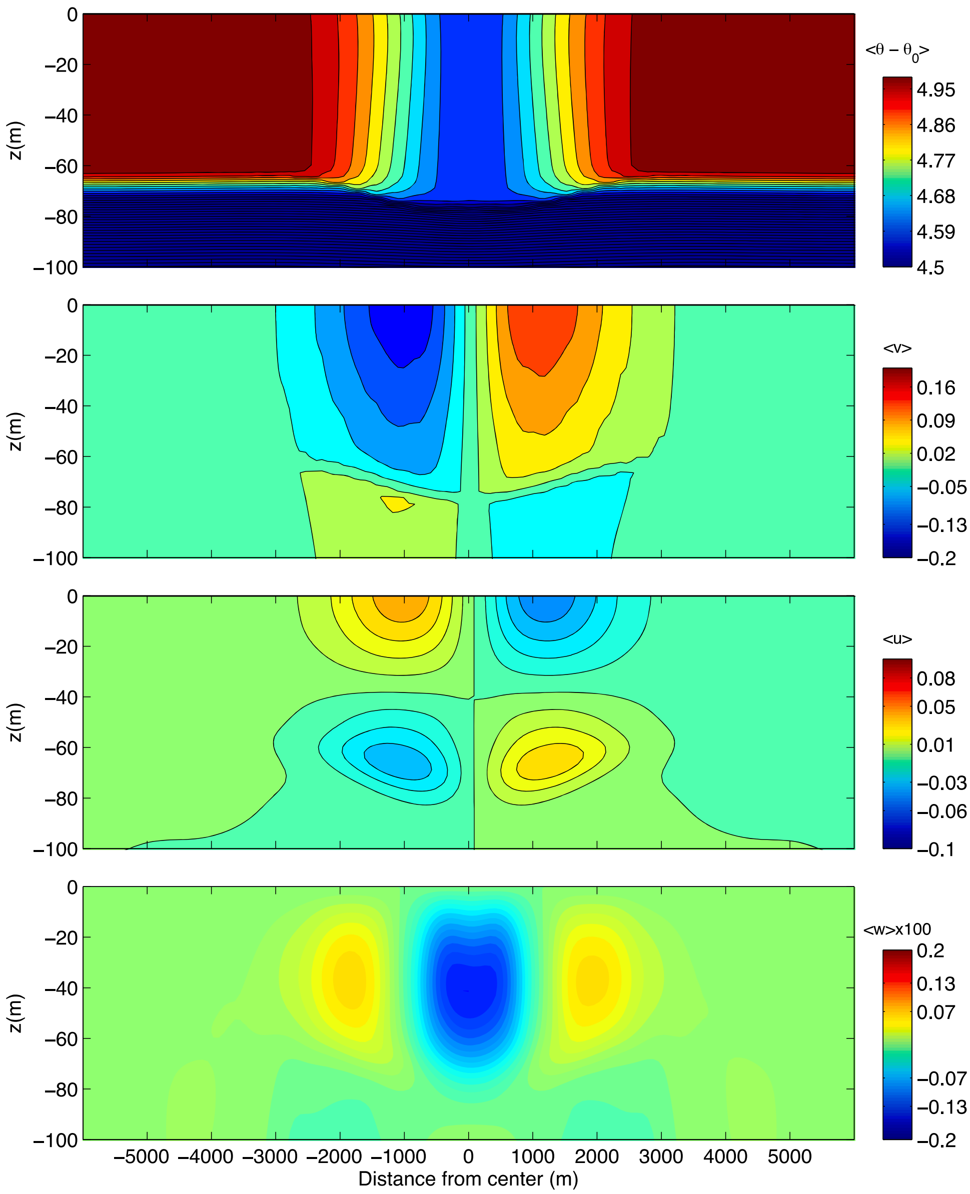

Fig. A3. Snapshots of averaged fields in an x–z plane for case C100 at simulation hour 2. The panels from top to bottom are: temperature anomaly ($\langle\theta - \theta_0\rangle$) in K, down-front velocity $\langle v\rangle$ in m s^{-1}, cross-front velocity $\langle u\rangle$ in m s^{-1} and vertical velocity $\langle w\rangle$ in m s^{-1}.

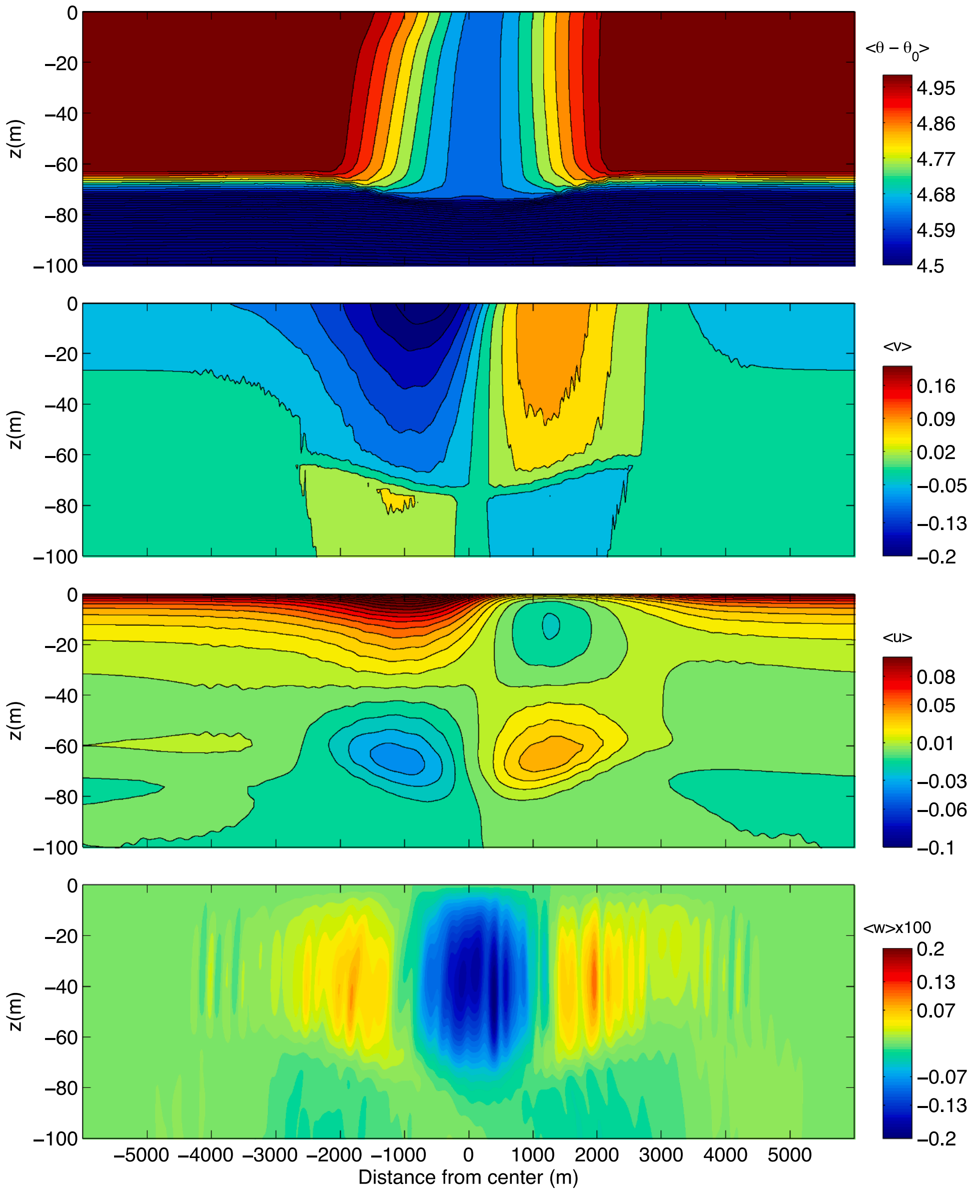

Fig. A4. Snapshots of averaged fields in an x–z plane for case E20 at simulation hour 2. The panels from top to bottom are: temperature anomaly ($\langle\theta - \theta_0\rangle$) in K, down-front velocity $\langle v\rangle$ in m s^{-1}, cross-front velocity $\langle u\rangle$ in m s^{-1} and vertical velocity $\langle w\rangle$ in m s^{-1}.

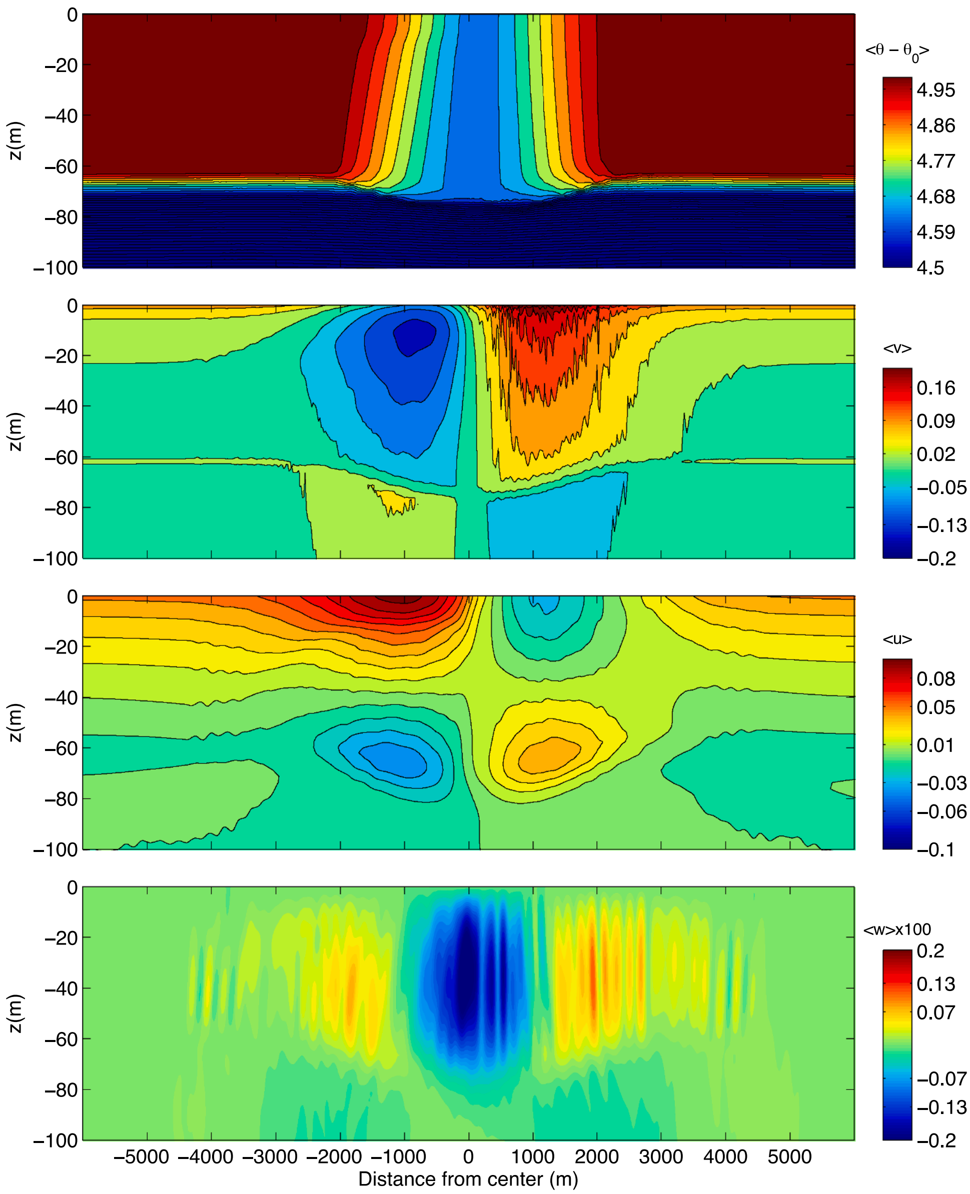

Fig. A5. Snapshots of averaged fields in an x–z plane for case N20 at simulation hour 2. The panels from top to bottom are: temperature anomaly ($\langle\theta - \theta_0\rangle$) in K, down-front velocity $\langle v\rangle$ in m s^{-1}, cross-front velocity $\langle u\rangle$ in m s^{-1} and vertical velocity $\langle w\rangle$ in m s^{-1}.

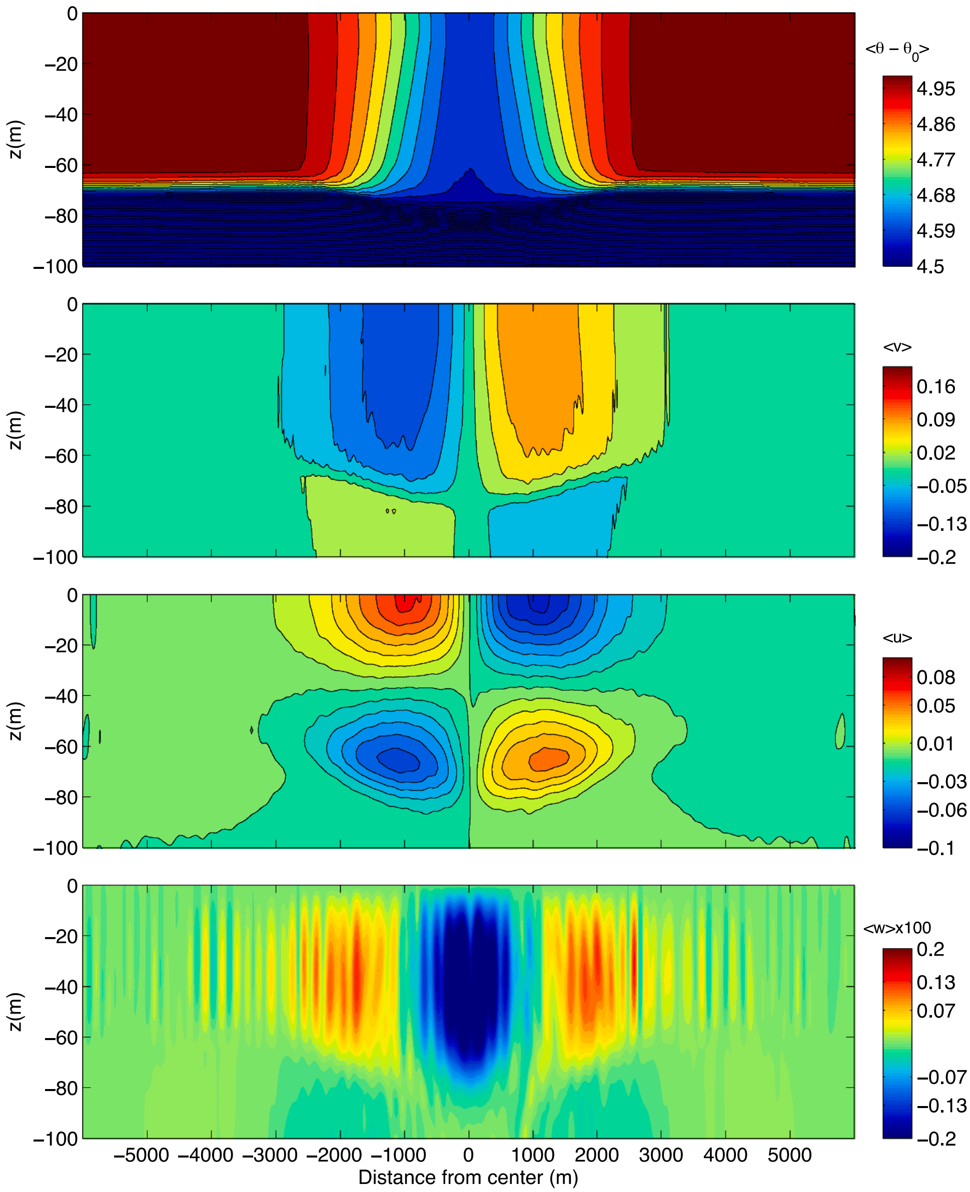

Fig. A6. Snapshots of averaged fields in an x–z plane for case C20 at simulation hour 2. The panels from top to bottom are: temperature anomaly ($\langle\theta - \theta_0\rangle$) in K, down-front velocity $\langle v\rangle$ in m s^{-1}, cross-front velocity $\langle u\rangle$ in m s^{-1} and vertical velocity $\langle w\rangle$ in m s^{-1}.

Appendix B. Parameterized Langmuir effect using the Kantha & Clayson mixing scheme

As discussed in Section 3.5, using the Harcourt (2015) parameterization to represent the effect of Langmuir turbulence through vertical mixing has some impact on frontogenesis, but the affect is much weaker compared to the profound changes observed in the LES model due to wave-current interaction. To investigate whether this phenomenon is generally applicable or specific to the Harcourt (2015) parameterization, a new set of experiments are conducted in this appendix utilized the Kantha & Clayson (2004) turbulent mixing scheme. That include the surface cooling case with cross- and along-filament surface wave forcing, as well as cross- and along-filament wind and wave forcing cases. In these experiments, the horizontal resolution is set to be 50 m, and C_{smag} is set to be 0.1.

The peak vertical vorticity for all four cases are compared between model results using the two mixing schemes in Fig. B1. The impact of surface gravity wave forcing through the Kantha & Clayson (2004) turbulent mixing scheme are weaker than the impact brought by the Harcourt (2015) parameterization for all four cases. The possible reason could be that, although the Kantha & Clayson (2004) parameterization has added both the breaking waves effect and the kinetic energy input from Langmuir circulations due to the presence of surface gravity waves in the TKE equation, the stability function in their model includes only the local forcing effect of stratification and shear, and missed the Stokes vortex force due to Langmuir circulation (Harcourt 2013). Harcourt (2015) fixed this problem and further introduced inhomogeneous press-strain rate and pressure-scalar gradient closures to the parameterization, and hence produces a strong Langmuir enhanced vertical mixing in the water column.

Also notice that the cross and along-filament wave forcing produce the same effect on frontogenesis for both mixing schemes. This is because the effect of Langmuir turbulence is parameterized and reflected in form of enhanced vertical mixing in both parameterizations. Although both parameterizations consider the wind-wave angle in the SMTC models, there is no wind forcing in the surface cooling case, and thus the direction of the wave makes no difference on the enhanced vertical mixing

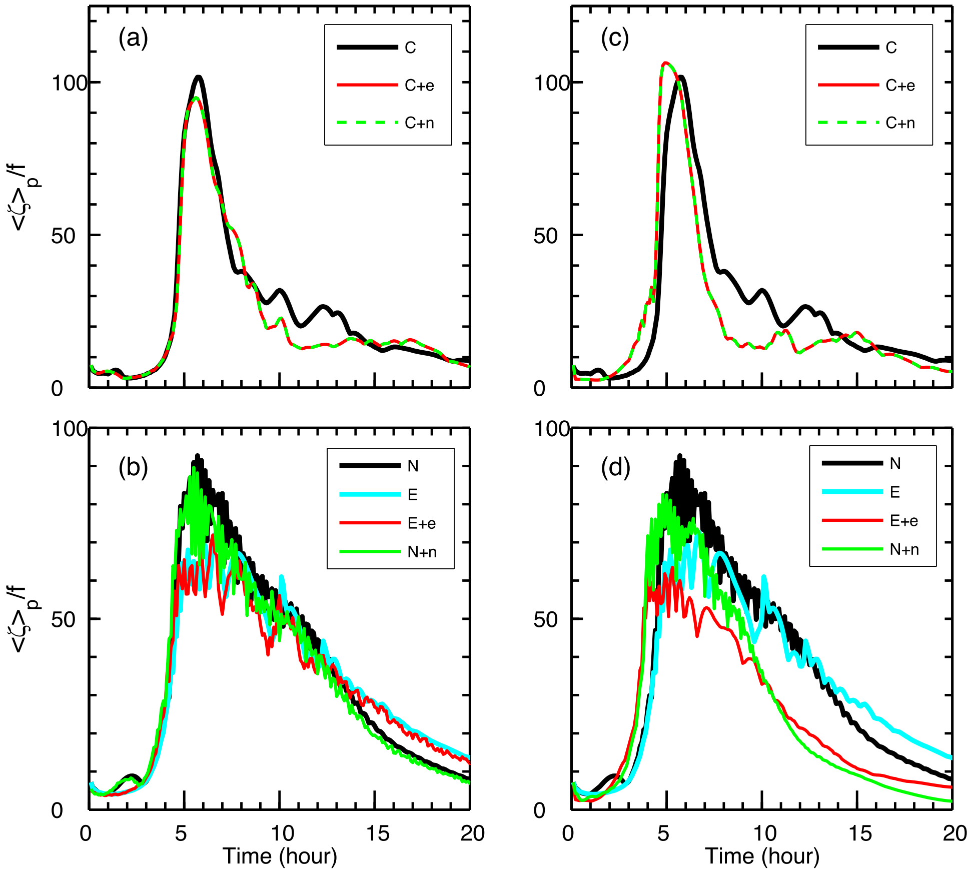

Fig. B1. Time variation of averaged normalized peak vertical vorticity $\langle\zeta\rangle_p/f$ near the water surface for NCOM simulations driven by surface cooling and waves (C; C + e; C + n) using (a) Kantha & Clayson (2004) mixing parameterization and (c) Harcourt (2015) mixing parameterization; and simulations driven by winds and waves (N; $N + n$; E; $E + e$) using (b) Kantha & Clayson (2004) mixing parameterization and (d) Harcourt (2015) mixing parameterization.

References

Abolfazli, E., Liang, J.H., Fan, Y., Chen, Q.J., Walker, N.D., Liu, J., 2020. Surface gravity waves and their role in ocean-atmosphere coupling in the Gulf of Mexico. J. Geophys. Res.: Oceans 125 (7) e2018JC014820.

Craik, A.D.D., Leibovich, S., 1976. A rational model for Langmuir circulations. J. Fluid Mech. 73, 401–426. https://doi.org/10.1017/S0022112076001420.

D'Asaro, E., Lee, C., Rainville, L., Harcourt, R., Thomas, L., 2011. Enhanced turbulence and energy dissipation at ocean fronts. Science (1979) 332, 318–322.

Fan, Y., Ginis, I., Hara, T., Wright, C.W., Walsh, E.J., 2009. Numerical simulations and observations of surface wave fields under an extreme tropical cyclone. J. Phys. Oceanogr. 39 (9), 2097–2116.

Fan, Y., Jarosz, E., Yu, Z., Rogers, W.E., Jensen, T.G., Liang, J.-H., 2018. Langmuir turbulence in horizontal salinity gradient. Ocean Model. 129, 93–103. https://doi.org/10.1016/j.ocemod.2018.07.010.

Fan, Y., Yu, Z., Savelyev, I., Sullivan, P.P., Liang, J.-H., Haack, T., Terrill, E., de Paolo, T., Shearman, K., 2020. The effect of Langmuir turbulence under complex real oceanic and meteorological forcing. Ocean Model. 149 https://doi.org/10.1016/j.ocemod.2020.101601.

Fan, Y., Yu, Z., Jacobs, G., 2021. Vertical coordinate and resolution dependence of the second moment turbulent closure models and their limitations. Ocean. Model. (Oxf) 168, 101896. https://doi.org/10.1016/j.ocemod.2021.101896.

Fan, Y., Rydbeck, A., Thoppil, P., Yu, Z., 2023. Numerical simulation of upper ocean responses to the passage of a Sumesoscale Eddy. Ocean. Model. (Oxf) 184 (2023), 102209. https://doi.org/10.1016/j.ocemod.2023.102209.

Ferrari, R., Rudnick, D.L., 2000. The thermohaline structure of the upper ocean. J. Geophys. Res. 105, 16,857–16,883.

GULA, J., MOLEMAKER, M.J., MCWILLIAMS, J.C., 2014. Submesoscale cold filaments in the Gulf Stream. J. Phys. Oceanogr. 44, 2617–2643.

Hakim, G., Snyder, C., Muraki, D., 2002. A new surface model for cyclone–anticyclone asymmetry. J. Atmos. Sci. 59, 2405–2420. https://doi.org/10.1175/1500469(2002)059.2405:ANSMFC.2.0.CO;2.

Hamlington, P.E., Van Roekel, L.P., Fox-Kemper, B., Julien, K., Chini, G.P., 2014. Langmuir–submesoscale interactions: descriptive analysis of multiscale frontal spindown simulations. J. Phys. Oceanogr. 44, 2249–2272. https://doi.org/10.1175/JPO-D-13-0139.1.

Harcourt, R.R., 2013. A second-moment closure model of Langmuir turbulence. J. Phys. Oceanogr. 43, 673–697. https://doi.org/10.1175/JPO-D -12-0105.1.

Harcourt, R.R., 2015. An improved second-moment closure model of Langmuir turbulence. J. Phys. Oceanogr. 45, 84–103. https://doi.org/10.1175/JPO-D -14-0046.1.

Holthuijsen, L.H., Tolman, H., 1991. Effects of the gulf stream on ocean waves. J. Geophys. 96, 12 755–12 771.

Hoskins, B.J., 1982. The mathematical theory of frontogenesis. Annu. Rev. Fluid Mech. 14, 131–151. https://doi.org/10.1146/annurev.fl.14.010182.001023.

Kantha, L.H., Clayson, C.A., 2004. On the effect of surface gravity waves on mixing in the oceanic mixed layer. Ocean Model. 6, 101–124.

Lapeyre, G., Klein, P., 2006. Impact of the small-scale elongated filaments on the oceanic vertical pump. J. Mar. Res. 64, 835–851. https://doi.org/10.1357/002224006779698369.

Large, W.G., McWilliams, J.C., Doney, S.C., 1994. Oceanic vertical mixing: a review and a model with a nonlocal boundary layer parameterization. Rev. Geophys. 32, 363–403. https://doi.org/10.1029/94RG01872.

Large, W.G., Patton, E.G., DuVivier, A.K., Sullivan, P.P., Romero, L., 2019a. Similarity theory in the surface layer of large-eddy simulations of the wind-, wave-, and buoyancy-forced southern ocean. J. Phys. Oceanogr. 49 (8), 2165–2187.

Lehahn, Y., d'Ovidio, F., Lévy, M., Heifetz, E., 2007. Stirring of the northeast Atlantic spring bloom: a Lagrangian analysis based on multisatellite data. J. Geophys. Res. 112, C08005. https://doi.org/10.1029/2006JC003927.

Li, Q., Fox-Kemper, B., 2017. Assessing the effects of Langmuir turbulence on the entrainment buoyancy flux in the ocean surface boundary layer. J. Phys. Oceanogr. 47, 2863–2886.

Liang, J.H., D'Asaro, E.A., McNeil, C.L., Fan, Y., Harcourt, R.R., Emerson, S.R., Yang, B., Sullivan, P.P., 2020. Suppression of CO_2 outgassing by gas bubbles under a hurricane. Geophys. Res. Lett. 47, 18. https://doi.org/10.1029/2020GL090249.

Mahadevan, A., 2006. Modeling vertical motion at ocean fronts: are nonhydrostatic effects relevant at submesoscales? Ocean. Model. (Oxf) 14, 222–240.

McWilliams, J.C., 2003. Diagnostic Force Balance and Its limits, Nonlinear Processes in Geophysical Fluid Dynamics. Kluwer Academic Publishers., pp. 287–304

McWilliams, J.C., Colas, F., Molemaker, M.J., 2009. Cold filamentary intensification and oceanic surface convergence lines. Geophys. Res. Lett. 36, L18602. https://doi.org/10.1029/2009GL039402.

McWilliams, J.C., Gula, J., Molemaker, M.J., Renault, L., Shchepetkin, A.F., 2015. Filament frontogenesis by boundary layer turbulence. J. Phys. Oceanogr. 45, 1988–2005. https://doi.org/10.1175/JPO-D -14-0211.1.

McWilliams, J.C., 2016. Submesoscale currents in the ocean. Proc. R. Soc. A 472, 20160117. https://doi.org/10.1098/rspa.2016.0117.

Mellor, G., 1998. A three-dimensional, primitive equation, numerical ocean model. Users Guide for the Princeton Ocean Model. Princeton Univ., Princeton, N. J, pp. 1–41.

Molemaker, M.J., McWilliams, J.C., Yavneh, I., 2005. Baroclinic instability and loss of balance. J. Phys. Oceanogr. 35, 1505–1517.

Rudnick, D.L., 1996. Intensive surveys of the Azorres front. Part II: inferring the geostrophic and vertical velocity fields. J. Geophys. Res. 101 (C7), 16291–16303.

Rudnick, D.L., Luyten, J., 1996. Intensive surveys of the Azores Front: 1. Tracer and dynamics. J. Geophys. Res. 101, 923–939. https://doi.org/10.1029/95JC02867.

Savelyev, I.B., Martin, P.J., Fan, Y., Savidge, D.K., Shearman, R.K., Haack, T., de Paolo, T., Terrill, E.J., Wang, Q., 2022. An empirical evaluation of turbulence closure models in the coastal ocean. J. Geophys. Res. Oceans 127. https://doi.org/10.1029/2021JC017588 e2021JC017588.

Smagorinsky, J., 1963. General circulation experiments with the primitive equations. I: the basic experiment. Mon. Wea. Rev. 91, 99–164.

Solano, M., Fan, Y., 2022. A new K-profile parameterization for the ocean surface boundary layer under realistic forcing conditions. Ocean. Model. (Oxf), 101958. https://doi.org/10.1016/j.ocemod.2022.101958.

Sullivan, P.P., McWilliams, J.C., 2018. Frontogenesis and frontal arrest of a dense filament in the oceanic surface boundary layer. J. Fluid Mech. 837, 341–380. https://doi.org/10.1017/jfm.2017.833.

Sullivan, P.P., McWilliams, J.C., 2019. Langmuir turbulence and filament frontogenesis in the oceanic surface boundary layer. J. Fluid Mech. 879, 512–553. https://doi.org/10.1017/jfm.2019.655.

Sullivan, P.P., McWilliams, J.C., 2024. Oceanic frontal turbulence. J. Phys. Oceanogr. 54, 333–358. https://doi.org/10.1175/JPO-D-23-0033.1.

Thomas, L.N., Tandon, A., Mahadevan, A., 2008. Submesoscale processes and dynamics. In: Hecht, M.W., Hasumi, H. (Eds.), Eddy Resolving Ocean Modeling, Geophysics Monogr. Series, vol. 177. AGU, Washington, D. C, pp. 17–38. https://doi.org/10.1029/177GM04.

Ullman, D.S., Cornillon, P.C., 1999. Satellite-derived sea surface temperature fronts on the continental shelf of the northeast US coast. J. Geophys. Res. 104 (C10), 23459–23478.

Yuan, J., Liang, J.-H., 2021. Wind- and wave-driven ocean surface boundary layer in a frontal zone: roles of submesoscale eddies and Ekman-Stokes transport. J. Phys. Oceanogr. 51, 2655–2680. https://doi.org/10.1175/JPO-D-20-0270.1.